ARTICLE

Check for updates

Water orientation and dynamics in the closed and open influenza B virus M2 proton channels

Martin D. Gelenter [1,2], Venkata S. Mandala [1,2], Michiel J. M. Niesen [1,2], Dina A. Sharon[1,2], Aurelio J. Dregni[1], Adam P. Willard[1] & Mei Hong [1✉]

The influenza B M2 protein forms a water-filled tetrameric channel to conduct protons across the lipid membrane. To understand how channel water mediates proton transport, we have investigated the water orientation and dynamics using solid-state NMR spectroscopy and molecular dynamics (MD) simulations. ^{13}C-detected water ^{1}H NMR relaxation times indicate that water has faster rotational motion in the low-pH open channel than in the high-pH closed channel. Despite this faster dynamics, the open-channel water shows higher orientational order, as manifested by larger motionally-averaged ^{1}H chemical shift anisotropies. MD simulations indicate that this order is induced by the cationic proton-selective histidine at low pH. Furthermore, the water network has fewer hydrogen-bonding bottlenecks in the open state than in the closed state. Thus, faster dynamics and higher orientational order of water molecules in the open channel establish the water network structure that is necessary for proton hopping.

[1] Department of Chemistry, Massachusetts Institute of Technology, Cambridge, MA, USA. [2] These authors contributed equally: Martin D. Gelenter, Venkata S. Mandala, Michiel J. M. Niesen, Dina A. Sharon. ✉email: meihong@mit.edu

W ater is ubiquitous in the interior of membrane proteins and co-regulates protein function. Substrate and ion transport by membrane proteins requires internal water molecules with the appropriate dynamics[1–3]. When water itself is transported, water–water hydrogen bonding dictates the rate of transport[4]. In contrast to most substrates and ions, protons are transported by water molecules as charge defects rather than atoms, by means of proton exchange and rapid rearrangement of water–water hydrogen bonds[5]. Transport of charge defects via this Grotthuss mechanism requires reorientation of water molecules and hydrogen bonds along the conduction pathway[6,7]. When the hydrogen bonding network is broken, for example, by polar amino acid residues in a protein, then proton transport can be prevented while water transport can remain, as in aquaporin[8,9]. When a protein channel contains more than a single file of water molecules and when proton conduction is predominantly unidirectional, then both water dynamics and water–water hydrogen bonding are expected to affect proton transport[10]. The interplay among water dynamics, water–water hydrogen bonding, and water orientation for proton transport is not yet well understood. This is partly due to the experimental challenges of determining atomic-resolution structures of membrane protein channels. Even when cryogenic-temperature crystal structures become available, usually only static snapshots of thermodynamically favored water are detected[9,11,12]. These snapshots reveal the oxygen positions of the structured water but not the disordered water, and the O–H bond orientation is usually unknown. In the absence of experimental data, molecular dynamics simulations have provided the main source of information about water dynamics and water orientation that underlie proton transfer[6,7,13].

The M2 protein of influenza viruses forms a water-filled proton channel[14] that serves as a model for understanding how proton transport is mediated by the dynamic structures of water and protein. M2's proton transport pathway is lined by four subunits of the transmembrane (TM) protein[15]. The channel is activated at low pH, when a central histidine residue becomes protonated[16]. Under this acidic condition, the histidine imidazolium rings, which are hydrogen-bonded to water, reorient on the microsecond timescale to shuttle protons from N-terminal water molecules to C-terminal water, causing proton flux into the virion[17,18]. A tryptophan (Trp) residue that is one helical turn away blocks the C-terminal protons from protonating the histidine, thus only allowing proton conduction from the N-terminus to the C-terminus[19–21]. Therefore, M2 transports protons using a mixed hydrogen-bonded chain between water and histidine. This detailed information about the histidine structure and dynamics in the influenza A M2 (AM2) protein was obtained from extensive solid-state NMR and crystallographic data[17,18,22–24]. In comparison, several aspects of the water structure and dynamics in the M2 pore have not been addressed. First, the water orientations in the closed and open channels are not known for M2, nor for most membrane proteins. Are water molecules partially oriented to permit Grotthuss hopping, and if so does the water orientation differ between the closed and open states? Second, it is not known how residues other than histidine affect the water–water hydrogen-bonding network. While AM2's pore-lining residues are nonpolar, the influenza B virus M2 protein (BM2) contains three serine residues along its pore-lining surface (Fig. 1). This polar surface might be expected to affect protein–water interactions and water–water hydrogen bonding, in turn changing the proton transport behavior. Third, for BM2, how water dynamics differ between the closed state and open state is not known.

To answer these questions, we have now conducted solid-state NMR experiments and MD simulations on membrane-bound
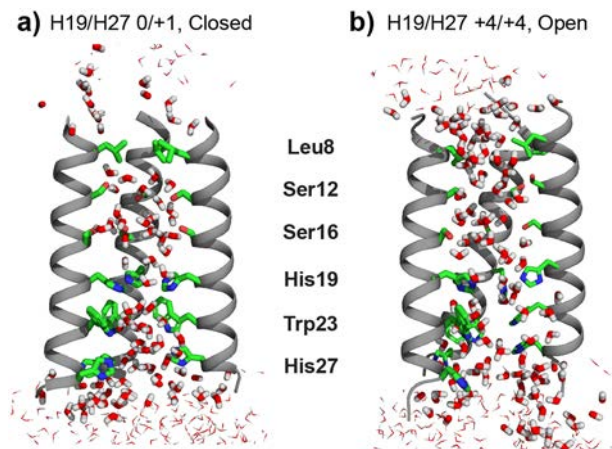

Fig. 1 Equilibrated BM2 structures in the POPE membrane. a Closed channel with the His19 and His27 tetrads in the 0 and +1 charge states, respectively, to mimic their protonation states at high pH. **b** Open channel with both His19 and His27 tetrads in the +4 charge state to mimic their protonation states at low pH. For clarity, only three out of four helices are shown. Pore-lining residues Leu8, Ser12, Ser16, His19, Trp23, and His27 are shown as sticks. Water in the channel lumen is shown as sticks while water outside the channel is shown as lines.

BM2. Solid-state NMR is an attractive method for obtaining experimental information about the dynamics and orientation of water molecules under biologically relevant conditions[25,26]. A direct comparison of water properties between the open and closed BM2 channels is possible due to our recently determined high-resolution structures of BM2 in lipid bilayers, where the 10 lowest-energy structures have a heavy-atom root mean-squared deviation of 1.5 Å[27]. These structures show that the four TM helices increase the tilt angle by 6° at low pH than at high pH, and the helices are on average 2.0 Å more separated from each other (Fig. 1). This uniform expansion of the BM2 pore at low pH correlates with the ability of BM2 to conduct protons bidirectionally, down the concentration gradient, like a canonical ion channel. In comparison, AM2's TM domain exhibits a helical kink at G34, which acts as a hinge to alternate water access to the N- or C-terminal halves of the pore[11,24]. This distinct conformational motion correlates with AM2's function to conduct protons strictly inward, like a transporter. On the basis of the open and closed BM2 structures, we now investigate the dynamics and orientations of water molecules in the BM2 pore. We conduct solid-state NMR experiments and MD simulations at 273–277 K, where both disordered and structured water molecules are present. We show that BM2's pore is several water molecules wide with many possible hydrogen-bonding pathways. Solid-state NMR data show that water in the low-pH BM2 channel exhibits faster reorientations as well as higher orientational order compared to the high-pH channel. This unexpected result suggests that water undergoes rapid small-amplitude reorientations to mediate proton conduction. MD simulations give consistent findings about the relationship between water orientation and dynamics, and indicate that this relationship is controlled by the proton-selective histidine residue.

Results
BM2 conducts protons at low pH, when the proton-selective histidine (H19) tetrad becomes protonated. A second, membrane-surface histidine (H27) is also protonated at low pH, but is not essential for proton conduction[28,29]. Experimentally, the closed and open states are accessible by controlling the pH of the membrane samples to pH 7.5 ("high pH") and pH 4.5 ("low pH"),

respectively. These conditions lead to average protonation states of 0/+1 for the H19/H27 tetrads at pH 7.5 and +4/+4 at pH 4.5, based on measured pK_a values[29,30]. For all-atom MD simulations of the solvated BM2 channel, we represent the closed and open channels by charge states of 0/+1 (closed[0/+1]) and +4/+4 (open[+4/+4]) for H19/H27, respectively, while the pH was not directly controlled. Simulations were initialized with the energy-minimized 1.5 Å experimental structures of BM2 tetramers in a POPE bilayer, matching experimental conditions (see Methods section; Supplementary Fig. 1a, b). Both charge states (Fig. 1) were stable, with Cα root mean-squared deviations (RMSDs) of 2.3–2.4 Å (Supplementary Fig. 1c, d). Channel-water dynamics were analyzed from four independent 100 ns MD trajectories for each channel. Below, we present findings from solid-state NMR experiments and MD simulations in parallel to facilitate comparison.

The BM2 channel pore is more hydrated at low pH than at high pH. We measured the amount of water in the high-pH and low-pH BM2 channels using ^{13}C-detected water ^{1}H polarization transfer experiments (Fig. 2a and Supplementary Fig. 2a). The water ^{1}H magnetization was selected by a soft ^{1}H excitation pulse followed by a 0.286-ms ^{1}H T_2' filter, then transferred to protein protons during a mixing time, τ_{mix}. The transferred magnetization was detected through protein ^{13}C signals[25,26]. All aliphatic ^{13}C intensities were integrated for the buildup curve analysis. The intensity ratio between spectra measured at short and long mixing times is inversely proportional to the protein–water distance (Supplementary Method, Eq. 7), whereas the relative intensities of the closed and open channels in the short-τ_{mix} limit reflect the relative magnitude of the product of the water amount and the square root of the effective spin diffusion coefficient (Supplementary Method, Eq. 5). This effective spin diffusion coefficient depends on both the chemical exchange rate and the ^{1}H spin diffusion coefficient[26,31]. It is known that chemical exchange between water and labile protein protons is slower at low pH than at high pH. For example, labile imidazole protons have hydrogen exchange rates of ~100,000 s^{-1} at pH 7.5 but only ~10,000 s^{-1} at pH 4.5[18,32], and the indole H^N proton of Trp has a hydrogen

exchange rate of ~10 s^{-1} at pH 7.5 but only ~0.1 s^{-1} at pH 4.5 (ref. [33]). Serine hydroxyls have similar hydrogen exchange rates at pH 4.5 and pH 7.5, but both are slow at ~300 s^{-1} (ref. [34]). Finally, exchange of protected amide protons with water is expected to be too slow to affect magnetization transfer on the millisecond timescale of τ_{mix} used here[35]. Despite the slower chemical exchange rates at low pH, the pH 4.5 BM2 sample shows faster polarization transfer buildup rates than the pH 7.5 sample (Fig. 2a, b and Supplementary Data 1), indicating that the low-pH channel pore contains more water[36,37]. The intensity ratios between the low-pH and high-pH samples extrapolate to 1.95 at vanishing τ_{mix} (Fig. 2c), indicating that the low-pH channel contains at least 1.95 times as much water as the high-pH channel.

MD simulations yielded both average and site-specific information about the number of water molecules in the open and closed states. We found that the open[+4/+4] BM2 channel contains 120 ± 7 water molecules from a channel-axis coordinate of −16 Å to +16 Å, while the closed[0/+1] channel contains 60 ± 5 water molecules (Fig. 2d and Supplementary Movie 1). Thus, the number of water molecules is 2.0 times higher in the low-pH channel than the high-pH channel (Fig. 2e), in excellent agreement with the experimentally measured ratio of water amounts. The number of water molecules increases the most near the hydrophobic valve formed by L8, and in the H19-W23 proton conduction motif. This increase in water density coincides with an increase in the channel diameter near those residues (Supplementary Fig. 1b).

Water motions are faster in the open channel than the closed channel. To investigate water dynamics in the low-pH and high-pH BM2 channels, we measured water protons' apparent transverse relaxation times (T_2') and rotating-frame relaxation rates ($R_{1\rho}$). The T_2' values are sensitive to picosecond (ps) to nanosecond (ns) motions while the $R_{1\rho}$ values are sensitive to microsecond (μs) to millisecond (ms) motions. These relaxation rates were measured at a sample temperature of 273 K to minimize chemical exchange between water and labile protein protons. Based on the composition of our membrane samples, about two
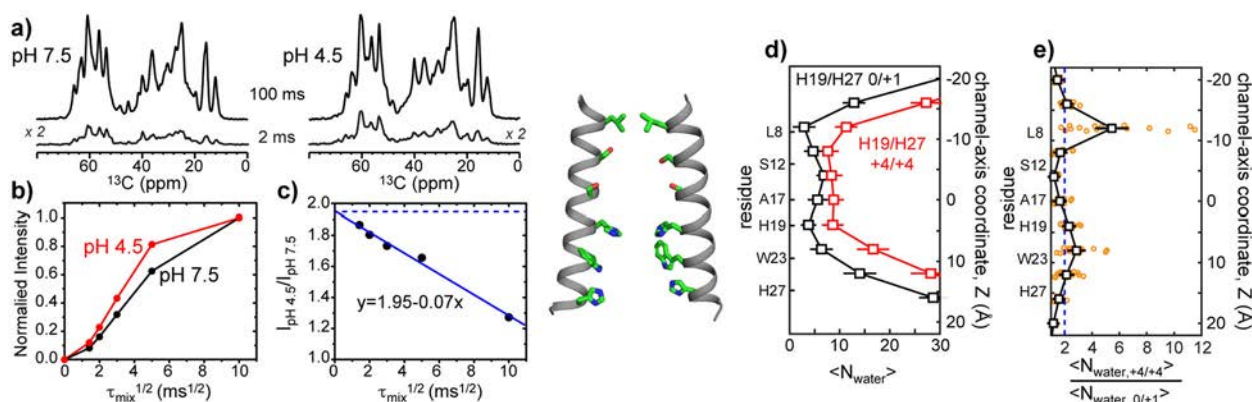

Fig. 2 Experimental and simulated water amounts in closed and open BM2 channels. a Water-transferred ^{13}C spectra with 2 ms and 100 ms ^{1}H mixing times at pH 7.5 and pH 4.5. Note the higher intensities of the 2-ms spectrum of the low-pH sample compared to the high-pH sample. **b** Normalized water-transferred intensity (S/S_0) as a function of mixing time τ_{mix}. The protein shows faster intensity buildup at low pH than at high pH. **c** Ratio of the low-pH versus high-pH water-transferred intensities as a function of ^{1}H mixing time. The ratio has an intercept of 1.95 (blue dashed line), indicating that the low-pH channel contains at least 1.95-fold more water than the high-pH channel. **d** Simulated average number of water molecules in 4 Å bins along the channel axis in the open (red) and closed (black) states. A ribbon view of the BM2 TM domain is shown on the left to illustrate the positions of key residues (sticks). For clarity, only two out of four TM helices are shown. **e** Ratio of the simulated number of water molecules for the open and closed states in 4 Å bins along the channel axis. On average, 2.0 times more water molecules are found in the open channel (blue dashed line), consistent with the experimental data. Black squares and error bars for simulations correspond to the mean and standard error of the mean for four independent trajectories. The data from the individual trajectories are shown as open orange circles.
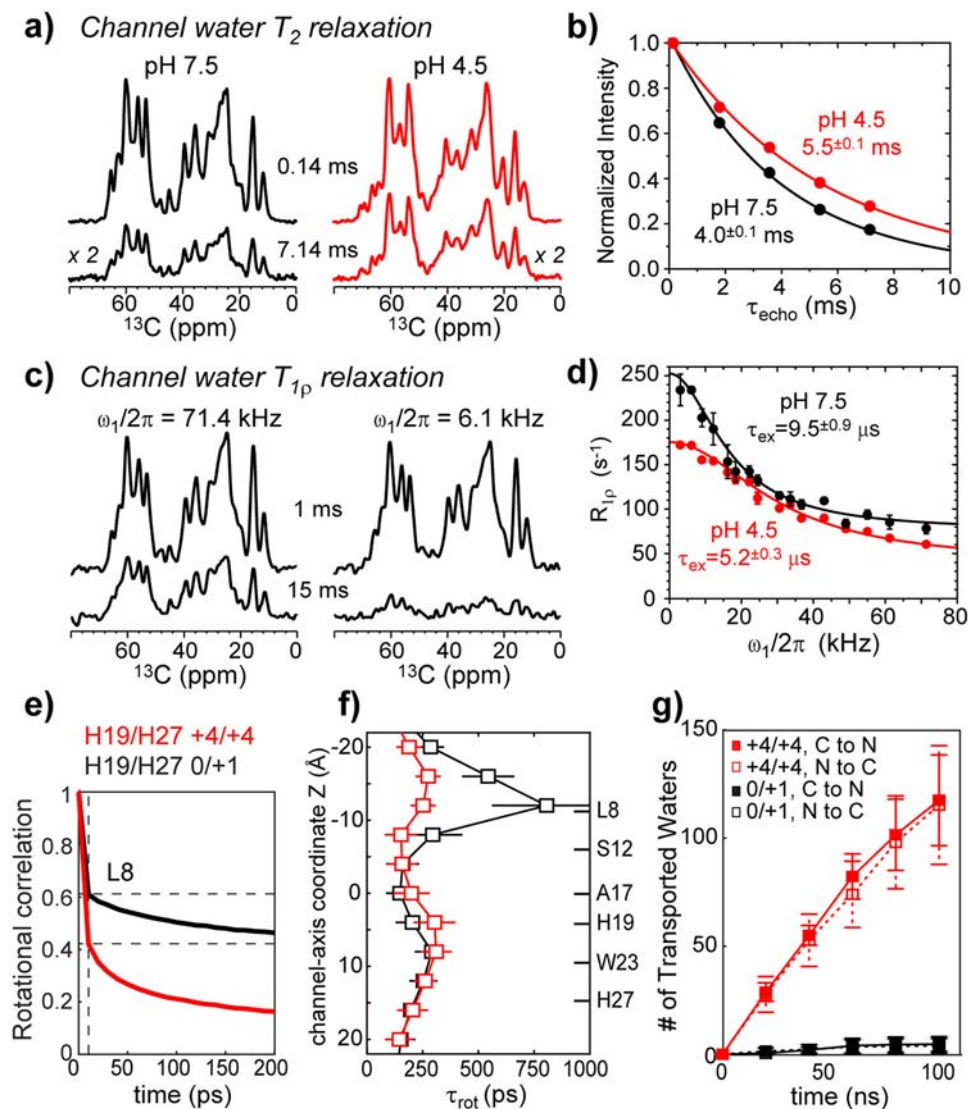
Fig. 3 Rotational and translational diffusion of water in BM2 channels. a Representative ^{13}C-detected NMR spectra probing water ^{1}H T_2' at pH 7.5 and pH 4.5. These spectra were measured with total echo delays of 0.14 ms and 7.14 ms. **b** Channel-water ^{1}H T_2' relaxation decay curves. T_2' relaxation is slower at low pH (red) than at high pH (black), indicating that the low-pH water has faster rotational dynamics. **c** Representative ^{13}C-detected NMR spectra of high-pH BM2 probing channel-water $R_{1\rho}$ relaxation. The spectra were measured with spin-lock times of 1 ms and 15 ms and spin-lock field strengths of 71.4 kHz (left) and 6.1 kHz (right). **d** On-resonance ^{1}H $R_{1\rho}$ relaxation dispersion profiles of water in the pH 7.5 (black) and pH 4.5 (red) channel. The low-pH channel shows a shorter τ_{ex} than the high-pH channel. Error bars for $R_{1\rho}$ values are the standard deviation of the fit for the signal decay at each spin-lock strength. **e** Simulated rotational correlation decay curves of waer near L8 in the closed and open channels. A fast decay in ~10 ps followed by a slower decay in ~500 ps is seen, and is representative of all water near protein residues. **f** Slow-component water rotational correlation times along the channel axis for closed and open BM2 channels. In the open state, water near H19 has the longest τ_{rot}. In the closed state, water near L8 has the longest τ_{rot}. **g** Total number of water molecules transported across the channel in both directions for the high-pH and low-pH states. Error bars for simulations are the standard error of the mean for four independent trajectories.

thirds of all water is bulk-like, one third is associated with the membrane surface, and only ~2% is within the channel[25]. We define bulk-like water as highly dynamic interlamellar water that does not exchange with the lipid headgroup or protein protons, but that is still not as mobile as isotropic bulk water. We used ^{1}H-detected NMR experiments to probe the dynamics of the bulk-like and lipid-associated water (Supplementary Fig. 3a, b) and ^{13}C-detected experiments to probe the dynamics of channel water near protein residues (Supplementary Fig. 2a, b).

At low pH, the ^{1}H-detected water T_2's are 48 ms for bulk-like water and 2.2 ms for lipid-associated water (Supplementary Fig. 3e and Supplementary Table 1). The fast relaxation of the lipid-associated water is consistent with retardation of water dynamics

by the membrane surface and chemical exchange of water protons with labile lipid headgroup protons. In comparison, ^{13}C-detected channel water displays an intermediate T_2' of 5.5 ± 0.1 ms at low pH (Fig. 3a, b), and the value decreases to 4.0 ± 0.1 ms at high pH. Transverse relaxation is driven by molecular tumbling[38], with slower relaxation indicative of shorter rotational correlation times (τ_{rot}). Because the channel-bound water has a small degree of orientational anisotropy (vide infra), coherent effects can accelerate the apparent transverse relaxation compared to that caused by molecular tumbling alone. Despite this coherent contribution, we can estimate an upper limit of τ_{rot} using the Bloembergen-Purcell-Pound (BPP) theory (Eq. 2, Methods section)[38]. The upper limit τ_{rot} values that correspond to these ^{13}C-detected water

^{1}H T_2''s are 5.5 ns for the low-pH water and 7.6 ns for the high-pH channel water. Both correlation times are an order of magnitude longer than the ^{1}H-detected bulk-like water τ_{rot} of 0.5–0.7 ns (Supplementary Table 1). Thus, the channel-water dynamics is highly restricted compared to bulk-like water. But even the bulk-like water in these hydrated liposomes is much less mobile than true bulk water, which has been reported to have a correlation time of 5.8 ps at 275 K[39]. We searched for residue-specific differences in the channel-water dynamics. However, even at a very short ^{1}H mixing time of 0.1 ms, all ^{13}C-detected ^{1}H T_2' values are similar, indicating that water translational diffusion and ^{1}H spin diffusion are rapid on this timescale, thus obscuring site-specific differences. Therefore, for the ^{13}C-detected water ^{1}H T_2' relaxation measurements, we used a 4-ms ^{1}H mixing time and integrated the aliphatic ^{13}C intensities to increase the sensitivity of the measurement.

To investigate slower dynamics of the channel water, we measured water ^{1}H $R_{1\rho}$ dispersion with protein ^{13}C detection, which distinguishes the protein-proximal channel water from bulk-like water and lipid-associated water (Fig. 3c and Supplementary Fig. 2b)[40]. If two water populations with different isotropic chemical shifts exchange on the µs to ms timescale, then $R_{1\rho}$ relaxation rates will vary with the spin-lock field strength in the kilohertz range. Relaxation is faster under weaker spin-lock field strengths and slower under stronger spin-lock fields. The intrinsic rotating-frame spin-lattice relaxation rate $(R_{1\rho}{}^0)$ is obtained in the limit of infinitely strong spin-lock fields[41]. Figure 3d shows that both the high-pH and low-pH channel water displays significant $R_{1\rho}$ dispersion in a spin-lock field strength range of 3–71 kHz. Fitting the profile using a two-state model[42] (Supplementary Method) yielded exchange time constants (τ_{ex}) of 5.2 ± 0.3 µs for the low-pH sample and 9.5 ± 0.9 µs for the high-pH sample. The fitting also yielded an exchange amplitude (ϕ_{ex}) of 2.6 ± 0.2 × 10^7 rad^{2}s^{-2} for the low-pH sample and 1.9 ± 0.2 × 10^7 rad^{2}s^{-2} for the high-pH sample. The exchange amplitude depends on the populations of the two states (p_1 and p_2) and chemical shift difference ($\Delta\omega$) according to $\phi_{ex} = p_1 p_2 \Delta\omega^2$. Assuming comparable populations, these τ_{ex} values indicate a ^{1}H chemical shift differences of ~2 ppm between the two populations of water. Based on considerations of the chemical exchange rates, we attribute the exchange process to that between two pools of water molecules in the channel pore (Supplementary Method)[43,44]. Importantly, this exchange process is 2-fold faster in the low-pH channel than in the high-pH channel. In comparison, bulk-like water shows no $R_{1\rho}$ relaxation dispersion while the lipid-associated water exhibits only minimal dispersion, which is independent of pH (Supplementary Fig. 3c, d, f). Finally, the intrinsic relaxation rate $R_{1\rho}{}^0$ is 2–10-fold faster for the channel water than the bulk-like and lipid-associated water (Supplementary Table 2), indicating that channel-water motion is more restricted than bulk-like and lipid-associated water[45,46].

MD simulations of water rotational dynamics are fully consistent with these experimental results. In both the open$^{+4/+4}$ and closed$^{0/+1}$ channel, the rotational correlation of water decays over two distinct timescales (Fig. 3e). We attribute the fast decay within ~10 ps to thermal motion of bulk-like water, and the slow decay to motion of the hydrogen-bonded water molecules in the confined pore and interactions of water with protein residues. Due to the time resolution used in the analysis of the MD simulations, we cannot further comment on the sub-10-ps rotational time, although it is possible that this motion is also affected by confinement within the channel[47,48]. The long-time relaxation component is slower for the closed$^{0/+1}$ state than the open$^{+4/+4}$ state, with an average τ_{rot} of 253 ± 12 ps for the closed channel and 223 ± 6 ps for the open$^{+4/+4}$

channel. Moreover, the slow-component's τ_{rot} values are not uniform throughout the channel (Fig. 3f): the slowest rotational dynamics is observed for water near L8 in the closed$^{0/+1}$ state and for water near H19 in the open$^{+4/+4}$ state.

We also examined water flux through the channel, by counting the number of water molecules that entered the channel on one side and exited at the other side (counted as one transport event). The open$^{+4/+4}$ channel transports 1.19 ± 0.24 water molecules per nanosecond (averaged over both directions) while the closed$^{0/+1}$ channel transports only 0.04 ± 0.03 water molecules per nanosecond (Fig. 3g and Supplementary Movie 1). The 30-fold reduction of the number of transported water molecules by the closed channel is striking. In addition, a water molecule takes 7.6 ± 0.2 ns on average to pass through the open$^{+4/+4}$ channel and 26 ± 3.4 ns to pass through the closed$^{0/+1}$ channel. The lifetime of an excess proton on hydronium ions is only a few ps[49]. Therefore, water translational diffusion through the channel is too slow to be the dominant process for proton transport, supporting the H19-mediated proton shuttling mechanism. We next computed the mean-squared displacement (MSD) of water molecules in the channel (Supplementary Fig. 4b), and fit it to the equation $MSD(t) = 6Dt^\alpha$, where the prefactor D corresponds to the water translational diffusion coefficient when the exponent $\alpha = 1$. We find that the water translational motion is sub-diffusive in both channels ($\alpha < 1$), but the dynamics are even slower in the closed$^{0/+1}$ state than in the open$^{+4/+4}$ state (Supplementary Fig. 4c). The differences in the water dynamics between the open$^{+4/+4}$ state and closed$^{0/+1}$ state are illustrated in Fig. 4 and Supplementary Fig. 5.

Water is more oriented in the open BM2 channel than in the closed channel. Water rotational diffusion can facilitate the making and breaking of hydrogen bonds. If the hydrogen-bonded network differs between the closed and open channels, then we would expect the water orientations to differ as well. In general, water in hydrated membranes is expected to be predominantly isotropic on NMR timescales. Even if there is anisotropy for the 2% of water that resides in the channel, this anisotropy is expected to be small and hence difficult to measure accurately by conventional lineshape experiments[50]. Therefore, we probed channel-water orientation using ^{1}H spin-lock recoupling experiments[51] (Supplementary Fig. 2c and Supplementary Fig. 3c). Using spin-lock rf field strengths (ω_1) that fulfill three recoupling conditions, $\omega_1 = 0.5\omega_r$, ω_r, and $2\omega_r$, where ω_r is the MAS frequency[52], we selectively recouple nuclear spin interactions. For water, at the $\omega_1 = \omega_r$ and $2\omega_r$ conditions, ^{1}H chemical shift anisotropy (CSA) is recoupled, while at the $\omega_1 = 0.5\omega_r$ and ω_r conditions, ^{1}H–^{1}H dipolar couplings are recoupled. The recoupled interactions should cause coherent oscillations of the time-dependent intensity decays, which can be fit to extract the motionally averaged anisotropies. The rigid-limit water ^{1}H CSA is 28.5 ppm[53], which corresponds to 22.8 kHz at 800 MHz, while the rigid-limit ^{1}H–^{1}H dipolar coupling within each water molecule is 35 kHz. As before, ^{13}C detection allows us to selectively detect water molecules inside the channel, near protein residues.

Figure 5a shows the ^{13}C-detected channel-water ^{1}H intensity decays under spin-lock recoupling. For both low- and high-pH samples, we observed clear oscillations at $\omega_1 = \omega_r$ and $2\omega_r$ but not at $\omega_1 = 0.5\omega_r$, indicating that the channel water has finite motionally averaged ^{1}H CSA but vanishing ^{1}H–^{1}H dipolar couplings. The latter can be understood by proton exchange between water molecules, which averages the intramolecular ^{1}H–^{1}H dipolar coupling. To verify that the oscillations at $\omega_1 = \omega_r$ and $2\omega_r$ are indeed due to ^{1}H CSA, we conducted the REfocused
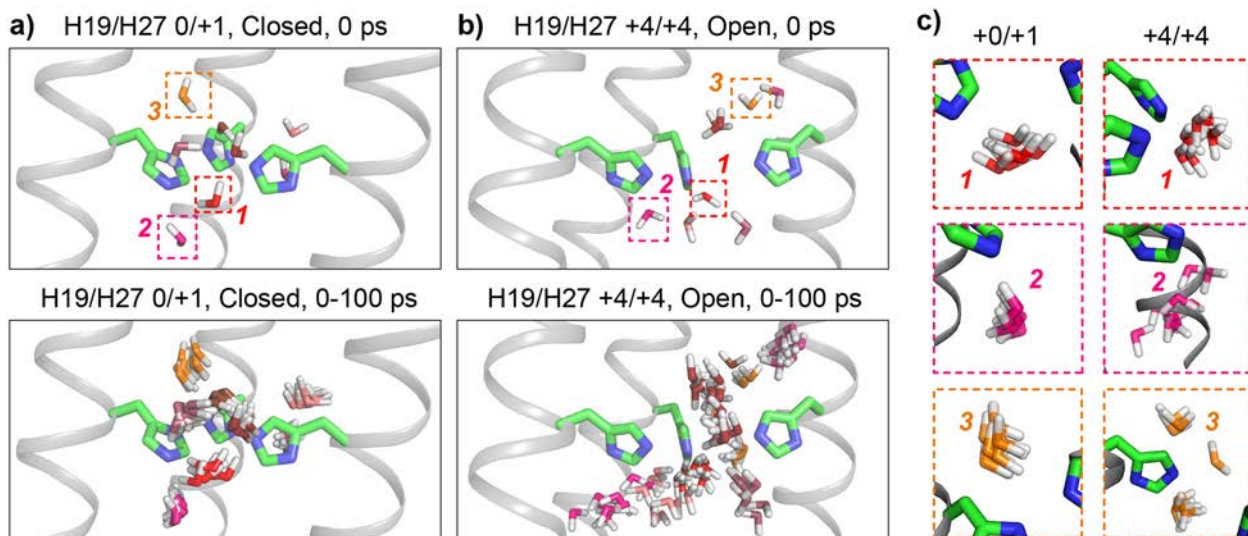
Fig. 4 Representative snapshots of rotational and translational diffusion of water molecules within 3Å of H19. a Water molecules near H19 in the closed$^{0/+1}$ channel. **b** Water molecules near H19 in the open$^{+4/+4}$ channel. The composite views at the bottom are taken in 10 ps steps over a 100-ps interval. For clarity, the oxygens of individual water molecules are colored differently. **c** Zoomed-in views of the trajectories of individual water molecules highlighted in **a** and **b**.

CSA Rotating-frame Relaxation (RECRR) experiment, which refocuses the CSA using phase-inverted spin-lock and 180° pulses (Supplementary Fig. 2d)[54]. Indeed, RECRR abolished most of the oscillations at $\omega_1 = \omega_r$ and $2\omega_r$ while retaining the same smooth decay at $\omega_1 = 0.5\omega_r$ (Fig. 5b), confirming that ^{1}H CSA is the main mechanism of the coherent oscillation.

To compare the channel-water anisotropy with the anisotropy of lipid protons and other water protons, we conducted the spin-lock recoupling experiments with ^{1}H detection (Supplementary Fig. 3). The lipid CH_2 and CH_3 protons exhibit coherent oscillations at $\omega_1 = 0.5\omega_r$ and ω_r but negligible oscillation at $\omega_1 = 2\omega_r$ (Supplementary Fig. 3g). This is consistent with the fact that lipid chains are anisotropically mobile and each CH_2 group has significant geminal ^{1}H–^{1}H dipolar couplings while the ^{1}H CSA is weak[55,56]. The total water ^{1}H signal in the ^{1}H spectra shows coherent oscillations at $\omega_1 = \omega_r$ and $2\omega_r$ but not at $\omega_1 = 0.5\omega_r$ (Supplementary Fig. 3f), similar to the ^{13}C-detected channel-water behavior, indicating CSA recoupling. However, the minima of the total water oscillations are much higher than the minima of ^{13}C-detected channel-bound water (Fig. 5a), indicating that only a fraction of all water is anisotropic. We attribute this anisotropy to water interacting with the membrane surface.

Importantly, the ^{13}C-detected ^{1}H spin-lock recoupling data indicate that the CSA-induced oscillation is faster at low pH than at high pH (Fig. 5a), indicating that the water orientational order is larger in the low-pH channel than in the high-pH channel. Although ^{1}H CSA is the dominant coherent effect for water, contributions from ^{1}H–^{1}H homonuclear dipolar couplings can speed up the dephasing at the ω_r recoupling condition[51]; therefore, we report CSA parameters extracted from the $2\omega_r$ matching conditions to compare the water CSAs between the high- and low-pH samples. Fitting the oscillations by numerical simulations (Supplementary Fig. 6) yielded a motionally averaged ^{1}H CSA of 1.8 ± 0.2 ppm at low pH and 1.2 ± 0.2 ppm at high pH for the $\omega_1 = 2\omega_r$ condition. These values correspond to order parameters S_{CSA} of 0.063 ± 0.007 at low pH and 0.042 ± 0.007 at high pH[53].

We next compared the simulated water orientational order with the experimental values by analyzing the O–H bond order parameter, S_{OH}, of water molecules in the MD simulations.

The principal axis of the water ^{1}H CSA is roughly colinear with the O–H bond, thus S_{CSA} is equivalent to S_{OH}. The average water S_{OH} value in the open$^{+4/+4}$ state is 0.039 ± 0.005, which is slightly larger than the average water S_{OH} value of 0.029 ± 0.004 in the closed$^{0/+1}$ state (Fig. 5c). Both values are in remarkably good agreement with the experimentally measured water S_{CSA} at high and low pH. The simulated S_{OH} values are dominated by water near a few residues, especially L8 and H19. To better understand these results, we extended our analysis by quantifying the water orientation in terms of the angle between the vector along the O–H bond and the channel axis (Fig. 5d). The site-resolved orientational averages (Figs. 5e and 6a and Supplementary Fig. 7) show that water in the closed$^{0/+1}$ channel displays little orientational preference except near L8, where there is a moderate preference for the oxygen-down orientation. In contrast, in the open$^{+4/+4}$ state, water orientational order is seen at almost all positions along the channel. Notably, this open$^{+4/+4}$ state orientational polarization is negative (oxygen pointing to the C-terminus) in the N-terminal half of the channel while positive (oxygen pointing to the N-terminus) in the C-terminal half of the channel (Figs. 5e and 6a and Supplementary Movie 1). This orientational switch occurs at H19. In other words, water molecules in the channel preferentially align with their oxygens pointing toward the charged H19 (Fig. 6c).

The closed$^{0/+1}$ and open$^{+4/+4}$ states differ in terms of the BM2 backbone conformation as well as the charge state of H19 and H27. To evaluate which of these factors cause the water anisotropy in the open$^{+4/+4}$ state, we conducted simulations in which the protein conformation was restrained to the low-pH solid-state NMR structure while the H19 and H27 charge states were assigned as 0/+1. Conversely, we restrained the protein conformation to the closed high-pH solid-state NMR structure while enforcing the +4/+4 charge state. These simulations show that the water anisotropy was abolished in the artificial open$^{0/+1}$ state despite the open protein conformation, while the orientational trend of oxygen-up C-terminal to H19 and oxygen-down N-terminal to L8 is maintained in the closed$^{+4/+4}$ state, despite the closed protein conformation (Fig. 5f). Therefore, the water orientational order is primarily controlled by the charge state of H19 and H27 tetrads, not the distances between helices.
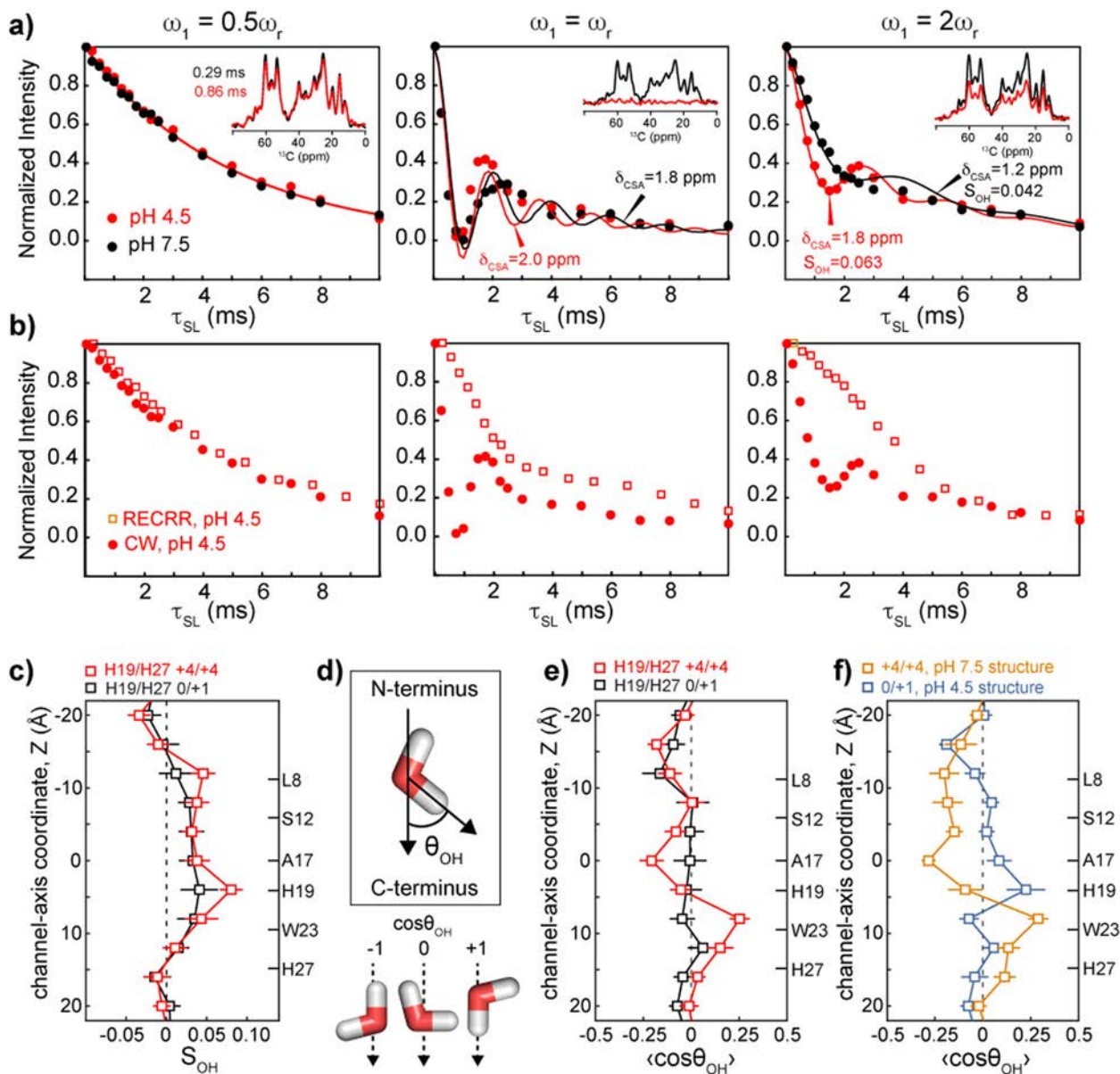
Fig. 5 Channel-water orientational order in BM2 from ^{13}C-detected ^{1}H spin-lock recoupling NMR experiments and MD simulations. a ^{13}C-detected water ^{1}H spin-lock recoupling data at $\omega_1 = 0.5\omega_r$ (left), ω_r (middle) and $2\omega_r$ (right). The spectral region integrated for each data point is shown in the inset for representative spin-lock times. Coherent oscillations are observed at ω_r and $2\omega_r$ but not at $0.5\omega_r$, indicating that ^{1}H CSA is the dominant anisotropic interaction. **b** Comparison of ^{13}C-detected water ^{1}H RECRR data (open squares) and CW spin-lock recoupling data (filled circles) at the three recoupling conditions. The oscillations are mostly removed by RECRR. **c** Simulated water OH-bond order parameter, S_{OH}, in the open and closed BM2 channels. **d** Definition of θ_{OH} and representative water orientations for $\cos\theta_{OH}$ values of -1, 0, and 1. Positive $\cos\theta_{OH}$ corresponds to water oxygen pointing to the N-terminus. **e** Time-averaged water $\cos\theta_{OH}$ values. Water has larger anisotropy in the open$^{+4/+4}$ channel than in the closed$^{0/+1}$ channel. An orientation change is observed at residue A17 at low pH. **f** Time-averaged $\cos\theta_{OH}$ of channel water when the $+4/+4$ state is restrained to the high-pH solid-state NMR protein structure (PDB: 6PVR) and the $0/+1$ state is restrained to the low-pH solid-state NMR structure (PDB: 6PVT). Positive $\langle\cos\theta_{OH}\rangle$ near W23 and negative $\langle\cos\theta_{OH}\rangle$ near L8 are observed for the $+4/+4$ state despite the high-pH structure. Error bars for simulations are the standard error of the mean for four independent trajectories.

^{13}C-detected ^{1}H spin-lock recoupling experiments conducted at lower temperatures produced identical recoupling curves (Supplementary Fig. 8b). Since chemical exchange and rotational motion are both slowed down at lower temperature, this data confirms that it is the charge state of histidine that controls water orientation anisotropy. Between the two histidines, H27 plays no role in controlling the water orientation, since no water anisotropy is seen near H27 in either $+1$ or $+4$ charge state (Fig. 5c–f and Supplementary Fig. 7). Thus, the orientational

order is induced by the spatially concentrated positive charge on the H19 tetrad.

Water hydrogen bonds are less interrupted in the open channel than in the closed channel. The presence of water orientational order within the open BM2 channel suggests that the water–water hydrogen-bonding network may be directional. To assess the possible influence of this directionality on proton transport, we counted the number of water–water hydrogen bonds and
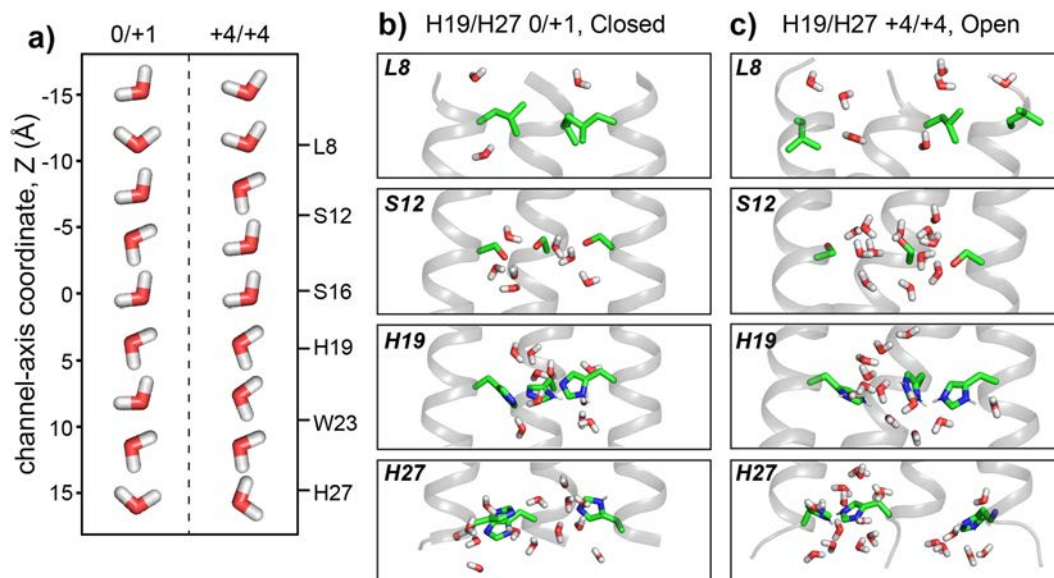
Fig. 6 Water orientations in the closed$^{0/+1}$ channel and the open$^{+4/+4}$ channel. a Most probable water orientations along the channel axis, plotted for 4 Å bins. **b**, **c** Representative snapshots of water in the **b** closed$^{0/+1}$ channel and the **c** open$^{+4/+4}$ channel. Only water within 3 Å of pore-facing residues are shown.
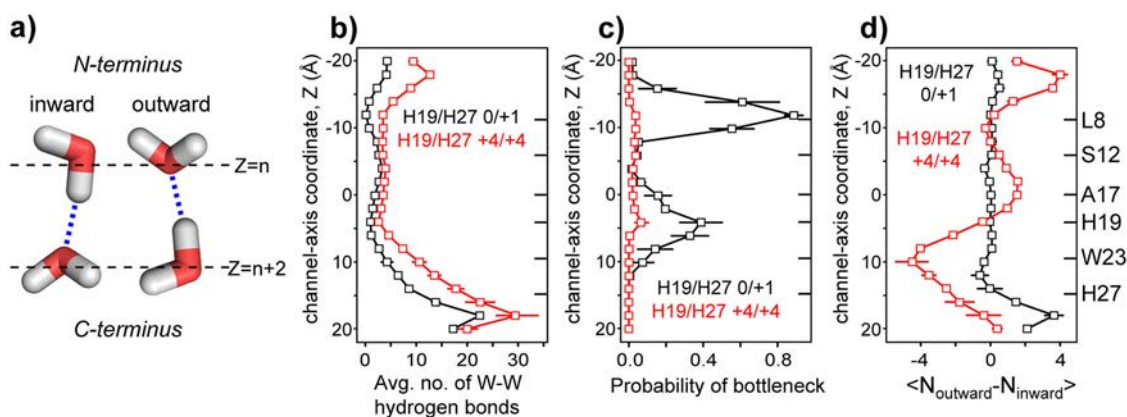

Fig. 7 Water–water hydrogen bonding in the closed and open BM2 channels. a Definition of the inward and outward water hydrogen bonds. **b** Average number of water–water hydrogen bonds along the channel axis. The open channel has more hydrogen bonds than the closed channel. **c** Probability of hydrogen-bond bottlenecks along the channel axis. The closed BM2 channel has high probabilities of bottlenecks at L8 and H19, while the open channel has low bottleneck probabilities throughout the channel. **d** Direction of water–water hydrogen bonds. The closed channel shows little preference for the hydrogen-bond polarity, while the open channel exhibits a bipolar hydrogen-bond orientation, reversed at H19. Error bars for simulations are the standard error of the mean for four independent trajectories.

evaluated their directions relative to the channel axis in the MD simulations (Fig. 7a, Methods section). We find that the open$^{+4/+4}$ state permits more water–water hydrogen bonds throughout the channel than the closed$^{0/+1}$ state (Fig. 7b). We classified hydrogen-bond bottlenecks as sites where connectivity along the channel was broken in an individual frame of the MD trajectory. Based on the statistics across 100 ns MD trajectories (Fig. 7c), we found two prominent bottlenecks, at L8 and H19, in the closed$^{0/+1}$ state, which are barriers to Grotthus-type proton transport. Bottlenecks are significantly more prevalent in the closed$^{0/+1}$ state, with at least one bottleneck in 97% of the frames, compared to only 24% of the frames in the open$^{+4/+4}$ state. On average, there are 3.7 bottlenecks in the closed$^{0/+1}$ state and 0.3 bottlenecks in the open$^{+4/+4}$ state. In addition, the water–water hydrogen bonds switch the directions in the open$^{+4/+4}$ state (Fig. 7d): the N-terminal half of the channel contains more

outward hydrogen bonds, while the C-terminal half contains more inward hydrogen bonds.

Discussion

These solid-state NMR data and MD simulations show that the water dynamics, orientation, and hydrogen-bonding in the BM2 channel differs significantly between low- and high-pH states. Low-pH channel activation gives rise to (1) a larger pore size with two-fold more water, (2) faster water reorientation and chemical exchange on the ns–µs timescales, and (3) higher water orientational order and more directional hydrogen bonds. Using ^{13}C detection of water ^{1}H polarization, we selectively detected the small population of water inside the BM2 channel. The fact that the low-pH channel contains more water is not surprising, since the four-helix bundle is more loosely packed at low pH due to

electrostatic repulsion between the four positively charged H19 residues[27,28]. The excellent agreement between the measured and simulated number ratio of water molecules in the closed and open channels validates both the NMR and simulation methods. Further, the larger amount of water is not an artefact of the low temperature (277 K) at which the experiments were conducted, as shown by control simulations at 297 K (Supplementary Fig. 10).

Interestingly, the number of water molecules in AM2 channels determined by X-ray crystallography was found to be sensitive to the experimental conditions. Initial cryogenic and room-temperature synchrotron crystal structures of AM2 found comparable or more water in the high-pH channel than in the low-pH channel[11]. The number of waters was much higher in the cryogenic structures than the room-temperature structures. These results were subsequently attributed to water ordering at low temperature and radiation damage at room temperature. When crystal structures were obtained at room temperature using an X-ray free-electron laser (XFEL), more water was found in the low-pH AM2 channel than the high-pH channel[10]. Solid-state NMR measurements at moderate temperatures represent a non-perturbing approach for quantifying the amount of water in membrane-bound channels. Interestingly, the XFEL data of AM2 also indicate a doubling of water amount at low pH compared high pH, in good agreement with the current BM2 results. This similarity of acid-activated water increase of AM2 and BM2 channels implies that the conserved histidine dictates the water amount in the pore (vide infra).

At high pH, simulated water densities indicate low water occupancy at L8 and H19 (Fig. 2d) and frequent bottlenecks in the water hydrogen-bonding network (Fig. 7c). This hydrogen-bond disruption is not observed in AM2, which contains unbroken chains of water–water hydrogen bonds from the N-terminus to the histidine tetrad at both high and low pH[11]. We attribute this difference to the different oligomeric structures of AM2 and BM2: AM2 adopts a more open N-terminal vestibule at high pH that is closed after acid activation[24,57]. The inter-conversion between the two conformations underlies the functional asymmetry of the AM2 transporter, where protons are exclusively conducted inward. In comparison, the BM2 tetramer structure undergoes a symmetric scissor-like motion with respect to the center of the TM domain[27]. This conformational symmetry has been proposed to explain the ability of BM2 to conduct weak outward proton current in addition to strong inward current. The lower water amount at L8 in the closed$^{0/+1}$ BM2 channel is thus correlated with a more compact N-terminal pore. The minimum diagonal heavy-atom distance at L8 is 11 Å for the open$^{+4/+4}$ channel and 5.5 Å for the closed$^{0/+1}$ channel (Supplementary Fig. 1b). BM2's H19 pK_a's have been measured and found to be significantly lower than the H37 pK_a of AM2[29]: the average pK_a of H19 is 5.1, while the average pK_a of H37 in AM2 is 5.9. Although the peripheral histidine, H27, speeds up proton release from H19, even an H27A mutant of BM2 still manifests a low average H19 pK_a of 5.6[28]. The current finding of a hydrogen-bond bottleneck at L8 provides a second mechanism of this depressed H19 pK_a's, as the interruption of the water wire at L8 will slowdown proton relay from the N-terminus to H19.

Both NMR relaxation and MD simulations indicate that water in the low-pH channel reorients more rapidly than water in the high-pH channel (Fig. 4, Supplementary Tables 1 and 2, and Supplementary Movie 1). Despite this faster dynamics, water in the low-pH channel has higher anisotropy than water in the high-pH channel (Fig. 5), as shown by larger motionally averaged ^{1}H CSA. Order parameters computed from simulations are in very good agreeement with the experimental data (Fig. 5c). The unexpected finding of faster water dynamics and higher water anisotropy can be rationalized by the fact that water molecules

that reorient quickly break and form hydrogen bonds with adjacent water molecules to permit proton exchange and thus Grotthuss hopping[5]. The higher water anisotropy at low pH is also fully consistent with the increased number and directionality of water–water hydrogen bonds at low pH (Fig. 7). This hydrogen bonding extends in opposite directions on either side of H19, with the C-terminal water favoring the inward hydrogen bonds and N-terminal water favoring outward hydrogen bonds. We attribute this hydrogen-bond polarity switch to the concentrated positive charge on the H19 tetrad.

The pH-dependent dynamics and orientations of BM2 channel water are surprisingly similar to the water properties in AM2 channels, despite the low sequence homology and the distinct oligomeric structures of the two proteins. AM2 also contains more dynamic water at low pH than at high pH, as manifested by picosecond time-dependent lineshapes in 2D IR spectra[58], longer water T_2' relaxation times[25], and a larger number of half-occupancy water molecules in crystal structures[10]. MD simulations of AM2 also indicated that the water hydrogen-bond direction switches above and below H37[11,13]. The fact that both channels exhibit faster water dynamics and a switch in hydrogen-bond direction at the proton-selective histidine at low pH suggests that the proton-selective histidine, without assistance from other pore-lining residues, controls the water amount, water anisotropy, and water wire directionality in both AM2 and BM2 channels. The ps–ns water reorientation and the µs histidine ring reorientation serve to complete the hydrogen-bonded chain to enable proton transfer.

The fact that the tetrameric conformation of M2 plays a lesser role in channel-water properties than the selectivity-filter residue is also supported by MD simulations that used a coiled-coil structure of BM2 solved in detergent micelles[59,60]. Despite the significant structural differences from the bilayer-bound structure[27], the simulations reached the same conclusion about increased pore size and pore hydration at low pH. The charge-flipped MD simulations shown here lend further support to the essential role of the H19 charge state for regulating the water-wire properties. When the H19 tetrad is neutral, even if the four-helix bundle is loosened, the number of water molecules and the water orientational order are low. Conversely, when the H19 tetrad is highly charged, even if the four-helix bundle is tightened, the water amount and orientational order increase significantly (Fig. 5f and Supplementary Fig. 9). Therefore, the polarity of the hydrogen-bond network is electrostatically controlled by the charge state of the histidine. For AM2, the protein conformation and dynamics play the roles of limiting the net proton flux and dictating the directionality of the proton flux[24,25]. Whether proton flux in BM2 is rate-limited by protein conformational dynamics has not been shown, but the similar rates of proton conduction and conserved HxxxW motif suggest that this may also be the case for BM2. The millisecond motion of the four-helix bundle accounts for the ~1000 s^{-1} proton flux of the M2 channels, while the symmetry of the helical motion affects the extent of the reverse proton current.

The combined measurements of water amount by polarization transfer NMR, water motional rates by relaxation NMR, and water orientation by recoupling NMR, represent a powerful approach for elucidating water properties in membrane proteins. MD simulations complement these NMR experimental results by providing site-specific information about water dynamics and hydrogen bonding. Our results show that proton conduction in the open state of BM2 is correlated with fast water rotational and translational diffusion, which optimizes the orientation of a hydrogen-bonded water wire[61,62]. The selectivity-filter histidine electrostatically controls water orientation and dynamics, and switches the water hydrogen-bond directions above and below

itself. The coexistence of dynamic disorder and orientational order of water may be a general property of channels and pumps that contain more than a single file of water molecules.

Methods

BM2 protein purification and membrane sample preparation. Uniformly ^{13}C and ^{15}N labeled BM2 (residues 1–51) was produced as described previously[27]. The protein sequence corresponds to the influenza B/Maryland/ 1/2001 strain (MFEPFQILSI CSFILSALHF MAWTIGHLNQ IKRGVNMKIR IKGPNKETINR). This construct contains the TM domain and a portion of the cytoplasmic domain of full-length BM2[63]. BM2 (1–51) was expressed as a SUMO-tagged fusion protein in *E. coli* BL21 (DE3) cells and purified using nickel affinity chromatography. The tag was then cleaved using SUMO protease, and the native BM2 was purified using preparative reverse phase HPLC.

Two BM2 samples bound to 1-palmitoyl-2-oleoyl-sn-glycero-3-phosphoethanolamine (POPE) membranes at pH 7.5 and pH 4.5 were used for study. Nearly identical ^{13}C and ^{15}N chemical shifts were observed for BM2 transmembrane residues in POPE, 1-palmitoyl-2-oleoyl-sn-glycero-3-phosphocholine: 1-palmitoyl-2-oleoyl-sn-glycero-3-phospho-(1′-rac-glycerol) (POPC:POPG) and 1,2-dilauroyl-sn-glycero-3-phosphoethanolamine (DLPE) membranes[27]. Since the bulk of the structure determination of BM2 in lipid bilayers was done with POPE lipid membranes, the two samples studied herein relied on this membrane. The protein:lipid molar ratio was 1:16, the protein mass was 8–9 mg for each sample, obtained from 3 L expression. The protein was reconstituted into the POPE membrane by organic solvent mixing as described before.[27] A Tris buffer (20 mM Tris-HCl, 2 mM ethylenediaminetetraacetic acid (EDTA), 0.2 mM NaN₃, and 2 mM TCEP) was used for the pH 7.5 sample while a citrate buffer (20 mM sodium citrate, 2 mM EDTA, 0.2 mM NaN₃, and 2 mM TCEP) was used for the pH 4.5 sample. The proteoliposomes were ultracentrifuged, dried to ~40 wt% water, then spun into 3.2 mm MAS rotors for solid-state NMR experiments.

Solid-state NMR experiments. Solid-state NMR experiments were conducted on a Bruker Avance II 800 MHz (18.8 T) spectrometer equipped with a triple-resonance ^{1}H/^{13}C/^{15}N Efree 3.2 mm magic-angle-spinning (MAS) probe. All experiments were carried out under 14 kHz MAS at a thermocouple-reported temperature of 263 K. The sample temperature was moderately higher due to frictional heating, and was estimated to be 273 K based on the water ^{1}H chemical shift[64]. Two-pulse phase modulation (TPPM) ^{1}H decoupling[65] was applied at an rf field of 71 kHz during ^{13}C acquisition. ^{13}C chemical shifts were referenced externally to the adamantane CH₂ chemical shift at 38.48 ppm on the tetramethylsilane scale and ^{1}H chemical shifts were referenced to the Hγ peak of 1-palmitoyl-2-oleoyl-sn-glycero-3-phosphocholine (POPC) at 3.26 ppm on the tetramethylsilane scale[66].

^{13}C-detected ^{1}H T_2' experiments (Supplementary Fig. 2a) started with the selection of water ^{1}H magnetization using a 1.5-ms Gaussian 90° excitation pulse, followed a variable echo period τ_{echo} containing a 7-µs 180° pulse in the middle. This τ_{echo} period was synchronized with the rotor period (τ_r) and ranged from 0.14 ms to 7.14 ms. For ^{1}H-detected T_2' measurements, τ_{echo} ranged from 0 to 714.3 ms. The water ^{1}H magnetization was transferred to protein with a spin diffusion mixing time τ_{SD} of 4 ms, followed by a CP contact time of 500 µs for ^{13}C detection. To ensure that all ^{1}H polarization detected originates from water, control experiments were conducted with a 0.1 ms τ_{mix}. No appreciable signal was observed with this mixing time (Supplementary Fig. 2a), indicating that all peptide signals, including the Hα signal that can overlap with water, were suppressed. ^{1}H spin diffusion buildup experiments used the same pulse sequence as the ^{13}C-detected ^{1}H T_2' experiments, with the echo delay fixed at 0.28 ms.

^{13}C-detected water ^{1}H $R_{1\rho}$ experiments (Supplementary Fig. 2b) started with water magnetization selection using a 1.5-ms Gaussian 90° excitation pulse. This was followed by a ^{1}H spin-lock pulse for a variable delay τ_{SL} with field strengths ($\omega_1/2\pi$) of 3 kHz to 71 kHz. A total of 16 rf field strengths were used, and τ_{SL} values ranged from 1 ms to 15 ms for each field strength. The water ^{1}H magnetization was transferred to protein with a τ_{mix} of 4 ms, followed by a CP contact time of 500 µs. To ensure that all ^{1}H polarization originates from water, control experiments were run with a 10-µs τ_{mix} and 1 ms spin-lock period. No appreciable signal was observed under these conditions, indicating that all peptide signals were suppressed and all ^{1}H polarization originates from water.

For spin-lock recoupling experiments (Supplementary Fig. 2c)[51], the $\omega_1/2\pi$ values were 7 kHz, 14 kHz, and 28 kHz, corresponding to matching conditions of $\omega_1 = 0.5\ \omega_r$, ω_r, and $2\omega_r$, and the τ_{SL} values ranged from 0.05 ms to 10 ms. The spin-lock field strength was optimized to achieve the best dephasing (lowest intensity) at a mixing time of 1 ms, which corresponds to the observed minimum for the ω_r condition and the initial fast decay for the $2\omega_r$ condition (Supplementary Fig. 7). For the ^{13}C-detected RECRR experiments (Supplementary Fig. 2d), the entire spin-lock period was separated into two phase-inverted portions, each containing a 180° pulse in the middle. The total $\tau_{SL} = 4n\tau_r$, where $n\tau_r$ is the duration of each sub-block. We used τ_{SL} values of 0.28–10.86 ms. The water ^{1}H magnetization was transferred to protein with a mixing time τ_{mix} of 4 ms, followed by a CP contact time of 500 µs. These RECRR experiments were conducted only at

spin-lock field strengths of 7 kHz, 14 kHz, and 28 kHz, using the same optimized field strengths as for the spin-lock recoupling experiments.

T_2' and $T_{1\rho}$ relaxation analysis. All spectra were processed in TopSpin (Bruker Biospin). NMR data analysis and fitting were conducted using MATLAB and OriginPro. ^{1}H- and ^{13}C-detected T_2' relaxation curves were fit to a biexponential function of the form:

$$I(\tau) = p_1 e^{-\tau/T_{2,1}'} + p_2 e^{-\tau/T_{2,2}'} \tag{1}$$

The two time constants and associated populations are reported in Supplementary Table 1. All error bars reflect a 68% confidence interval.

The rotational correlation time τ_{rot} is obtained from the water ^{1}H T_2' values using the Bloembergen−Purcell−Pound (BPP) theory[38] as follows:

$$\frac{1}{T_2} = \frac{3\mu_0^2\gamma^4\hbar^2}{320\pi^2 r^6}\left(3\tau_c + \frac{5\tau_{rot}}{1 + \omega_0^2\tau_{rot}^2} + \frac{2\tau_{rot}}{1 + 4\omega_0^2\tau_{rot}^2}\right) \tag{2}$$

Here μ_0 is the magnetic permeability of free space, γ is the ^{1}H gyromagnetic ratio, $\hbar$ is the reduced Planck's constant, r is the intramolecular ^{1}H–^{1}H distance of water (1.58 Å), τ_{rot} is the rotational correlation time, and ω_0 is the proton Larmor frequency which is $2\pi \times 800 \times 10^6$ rad/s in a magnetic field of 18.8 T.

^{13}C-detected water ^{1}H $R_{1\rho}$ decays were fit to variable-amplitude single exponential functions. The $R_{1\rho}$ rates at ω_1 values away from the three recoupling conditions ($\omega_1 = 0.5\omega_r$, ω_r, and $2\omega_r$) were used for the relaxation dispersion analysis. These $R_{1\rho}$ values were fit to Eq. (3), which assumes a two-state exchange model[40,42]:

$$R_{1\rho} = R_{1\rho}^0 + \frac{\phi_{ex}(1/\tau_{ex})^2}{\omega_1^2 + (1/\tau_{ex})^2} \tag{3}$$

Here $R_{1\rho}^0$ is the rotating-frame spin-lattice relaxation rate in the limit of infinitely strong ω_1. The exchange parameter $\phi_{ex} = p_1 p_2 \Delta\omega^2$ depends on the populations of the two states, p_1 and p_2, and on the isotropic chemical shift difference $\Delta\omega$ between the two states. τ_{ex} is the exchange time constant and ω_1 is the rf spin-lock field strength. Fitting the $R_{1\rho}$ dispersion profile to Eq. (3) requires that the relaxation dispersion is solely due to fast exchange between two different isotropic chemical shifts.

Numerical simulations of spin-lock recoupling to extract ^{1}H chemical shift anisotropy. The ^{13}C-detected water ^{1}H $R_{1\rho}$ rates at the three recoupling conditions cannot be fit to an exponential function because they exhibit an additional fast oscillating component due to coherent contributions. We simulated these curves using the SpinEvolution software[67]. The simulations utilized an eight-spin system consisting of the protons in four hydrogen-bonded water molecules (Supplementary Fig. 6a)[68]. Numerical simulations were run using the NMR experimental conditions, including a static magnetic field of 18.8T (800 MHz), an MAS frequency of 14 kHz, and a ^{1}H carrier frequency set to be on-resonance with the water protons. These simulations began with ^{1}H magnetization along the x-axis, and the amount of magnetization was monitored with increasing spin-lock times (Supplementary Fig. 6b). Motionally averaged dipolar order parameters S_{HH} between the two water protons were varied by setting the dipolar couplings to be 5% of the rigid-limit coupling. Motionally averaged ^{1}H CSA was varied and compared with the rigid-limit water ^{1}H CSA of 28.5 ppm[53]. The results of the simulations were found to be insensitive to the ^{1}H CSA tensor orientation, thus we set $\alpha = \beta = \gamma = 0°$. We note that when ^{1}H CSA is included but ^{1}H–^{1}H dipolar couplings are turned off, the eight-spin simulation reverts to a single-spin situation.

The water ^{1}H spin-lock recoupling data exhibit oscillations that are significantly dampened compared to what is expected for a single CSA magnitude subjected to homogeneous B_1 irradiation (Supplementary Fig. 6c). This dampening is likely due to a combination of incoherent $R_{1\rho}$ relaxation, B_1 field inhomogeneity, and a distribution of ^{1}H CSAs. We are unable to differentiate the effects of B_1 field inhomogeneities from the effects of CSA distribution. Thus, we assume that there is a single dominant motionally averaged CSA. To fit the measured spin-lock recoupling profile, the B_1 inhomogeneity for a ^{1}H loop-gap resonator[69] was modeled as such: CSA experiments were simulated for rf spin-lock field strengths corresponding to 90–100% in 0.2% increments of the recoupling conditions $0.5\omega_r$, ω_r, and $2\omega_r$. We note that an rf field inhomogeneity of 110-100% results in approximately the same dephasing curve as an rf inhomogeneity of 90–100%, e.g., dephasing is roughly symmetric about the matching condition. These were then multiplied by a polynomial weighting function, $(\Delta\omega_1/\Delta\omega_{1,max})^4$ to account for the fact that the majority of the sample experiences the desired spin-lock field strength, while the contribution from spin-lock fields that are 10% different from the desired value is relatively small (Supplementary Fig. 6d). The weighted coherent decay curves were summed and normalized to one, before being multiplied with an exponential decay function with a time constant of 5 ms to account for the incoherent $R_{1\rho}$ relaxation components. The RMSD between the measured and simulated spin-lock recoupling curves was calculated to find the best-fit motionally averaged CSA for each recoupling curve (Supplementary Fig. 6e).

System setup and molecular dynamics simulation protocols. Initial systems for the MD simulations were set up using CHARMM-GUI[70] using the following steps. First, pore waters were added to the lowest-energy NMR structures (residues 1–33) of the closed (6PVR) and open (6PVT) BM2 channels[27], using the DOWSER package[71], which omitted a drain step to prevent the dehydration of the cavity. The C-terminal residue R33 was capped with a methyl group and hydrogens were added using CHARMM-GUI[70]. The charge states of H19/H27 were assigned as 0/+1 for the high-pH helix bundle and +4/+4 for the low-pH helix bundle. Next, the prepared BM2 structures, including the pore water molecules, were inserted into an 80 Å × 80 Å POPE bilayer containing 190 lipids, orienting the channel-axis perpendicular to the membrane plane. The bilayer was solvated with a 30-Å-thick water layer on each side of the bilayer with 150 mM NaCl. The boundaries of the simulation systems were handled using periodic-boundary conditions. The system was energy-minimized using 5000 steps of steepest descent and equilibrated at 297 K and 1 atm. The equilibration protocol consisted of a series of short simulations (375 ps in total) with harmonic position restraints on the protein backbone (BB), protein sidechains (SC), lipid headgroups (LH), and lipid tails (LT; harmonic restraints as specified in Supplementary Table 3). The equilibrated structures were next subjected to four independent production runs of 130 ns in an NPT ensemble, with semi-isotropic pressure coupling at 1 atm, using a Parrinello-Rahman barostat[72,73] and 277 K, using the V-rescale thermostat[74]. This temperature was chosen to mimic the experimental temperature of ~273 K. All water analysis was performed on the last 100 ns of MD trajectories, leaving out the first 30 ns of unconstrained NPT simulation as equilibration. All simulations were carried out using GROMACS 2018.3[75] and the CHARM36 forcefield, using the TIP3P water model. Short ranged non-bonded interactions employ a 1.2-nm cut-off, long-range electrostatics were calculated using the smooth particle mesh Ewald (PME) method. The LINCS algorithm[76] was used to constrain h-bonds and to enable stable integration using a 2 fs timestep, simulation snapshots were saved every 10 ps for analysis.

Although the TIP3P water model has been used for peptide and small protein simulations below room temperature[77,78], we note that there are known limitations on the accuracy of TIP3P at 277 K[79]. Therefore, we performed control simulations at 297 K to reproduce the analysis (Supplementary Fig. 10). The simulations at 297 K yield qualitatively comparable results to those at 277 K. Importantly, we still find increased water density (Supplementary Fig. 10a, b), water dynamics (Supplementary Fig. 10c, d), water order (Supplementary Fig. 10e–g), and hydrogen bonding (Supplementary Fig. 10h–j) in BM2 at pH 4.5 compared to BM2 at pH 7.5.

While most water analysis was conducted on unrestrained simulations, additional simulations were carried out where the protein structure was restrained to the solid-state NMR backbone structure using harmonic restraints (50 kJ mol⁻¹ nm⁻² force constant). Specifically, control simulations were performed in which the open BM2 (+4/+4 H19/H27 charge state) was kept near its NMR structure (PDB: 6PVT) and the closed BM2 (0/+1 H19/H27 charge state) was kept near its NMR structure (PDB: 6PVR). These restrained simulations had dilated channels compared to the unrestrained simulations (Supplementary Fig. 1b), thus giving a larger number of channel-water molecules and slightly increased translational and rotational dynamics. However, the ratio of water molecules between the +4/+4 and +0/+1 H19/H27 charge states, the increased water mobility for the +4/+4 charge state, and the orientation anisotropy for the +4/+4 charge state, were preserved (Supplementary Fig. 4a). Additional restrained simulations that investigate the effect of the H19/H27 charge state on water-orientation, in the absence of large-scale conformational changes in BM2, (Fig. 5f and Supplementary Fig. 9) restrain the open BM2 to its NMR structure (PDB: 6PVT) while using the closed BM2 charge state (0/+1 H19/H27), and restrain the closed BM2 to its NMR structure (PDB: 6PVR) while using the open BM2 charge state (+4/+4 H19/H27).

Analysis of the MD channel-water trajectories. The water correlation times, orientation, and hydrogen bonding in the last 100 ns of each simulation were analyzed using the MDAnalysis package[80]. The scripts for calculating these quantities from the MD trajectories are available via github (https://github.com/mjmn/BM2-MD). Reported values and error bars represent the mean and standard error of the mean, over the independent trajectories included in calculating the reported quantity.

Channel-axis coordinate, Z. The channel-axis coordinate, Z, is defined as the projection onto a vector along the principal axis of the Cα atoms in the BM2 channel, with the vector origin set to the center of the four A17 Cα atoms, and the positive direction oriented towards the C-terminus of BM2 (channel-axis vector). To assign Z values to residues, we use the average Z value of all heavy atoms in the corresponding residue over the combined trajectories (Supplementary Table 4).

Water density. Water density is reported as the average number of water molecules within a 4-Å bin along the Z axis. Water molecules are assigned based on the position of their oxygen atom. Only water molecules that are within 15 Å of the channel-axis vector are included. Restraining the protein backbone to the solid-state NMR structure resulted in slightly more water within both the open and closed channels, but the ratio between the amount of water in each channel

remained the same (Supplementary Fig. 4a). This is due to the fact that the equilibrated structures are somewhat constricted compared to the solid-state NMR structures (Supplementary Fig. 1b).

Water rotational dynamics. Rotational auto-correlation functions are calculated as

$$C_{\mu}(\tau) = \frac{1}{2} \langle 3\left[\boldsymbol{\mu}(t) \cdot \boldsymbol{\mu}(t+\tau)\right]^2 - 1 \rangle_t \tag{4}$$

where $\boldsymbol{\mu}(t)$ is the orientation of the water-molecule dipole vector at time t. Fitting the long-time decay (>10 ps) of the auto-correlation function to an exponential function gives the rotational correlation time τ_{rot}:

$$C_{\mu}(\tau) \propto e^{-\tau/\tau_{\text{rot}}} \tag{5}$$

The τ_{rot} value was determined as a function of the displacement along the channel axis by assigning each water molecule to the channel-axis coordinate bin (4 Å width) at which its oxygen atom resides at $\tau = 0$.

Water translational dynamics. The translational dynamics of water is quantified by fitting the mean-square displacement, MSD,

$$\text{MSD}(\tau) = \left\langle \left| \mathbf{r}(t+\tau) - \mathbf{r}(t) \right|^2 \right\rangle_t \tag{6}$$

to the following function:

$$\text{MSD}(t) = 6Dt^{\alpha} \tag{7}$$

where $\boldsymbol{r}(t)$ is the position of a water oxygen at time t, and α, and D are parameters that define the translational motion of water. In the BM2 channel, the water dynamics were found to be sub-diffusive (i.e., $\alpha < 1$). This quantity was determined as a function of the displacement along the channel axis.

The flux of water molecules across the channel was calculated from both the N-terminus and the C-terminus by counting the number of water molecules that enter the channel on one side and exit on the other side. A water molecule contributes to the flux at the time it exits the channel. For a given water molecule, it is labeled as: entering the channel on the N-terminal side when it crosses the two-dimensional plane defined by $Z = -20$ Å in the positive Z direction, exiting the channel on the N-terminal side when it crosses the $Z = -20$ plane in the negative Z direction, entering the channel on the C-terminal side when it crosses the two-dimensional plane defined by $Z = 20$ Å in the negative Z direction, and exiting the channel on the C-terminal side when it crosses the $Z = 20$ Å plane in the positive Z direction. No significant difference in $D(Z)$ was found between the closed and open channel. The slowdown in translational dynamics in the closed channel, summarized here using only the coefficient, is also apparent from MSD versus time plots (Supplementary Fig. 4b) and in the total number of transported water molecules through the channel: this number is 2.73 ± 0.41 molecules/ns in the open channel and 0.08 ± 0.05 molecules/ns in the closed channel (Fig. 3g).

Water orientation. The water orientational order in the channel was determined by analyzing the probability distribution of the dot product between the water OH-bond vector and the channel-axis vector, Z. The full probability distributions, $P(\cos(\theta_{\text{OH}}))$, are shown in Supplementary Fig. 7. Several quantities derived from these probability distributions are presented in the main text and are described here.

We used the average value $\langle\cos(\theta_{\text{OH}})\rangle$ to assess the orientational preference of water along the channel axis (Fig. 5e). This quantity is defined as:

$$\langle\cos(\theta_{\text{OH}})\rangle(Z) = \int_{-1}^{1} \cos(\theta_{\text{OH}}) P(\cos(\theta_{\text{OH}})|Z) d\cos(\theta_{\text{OH}}) \tag{8}$$

To compare with the measured order parameters more directly, we also calculated the OH-bond vector order parameter according to:

$$S_{\text{OH}}(Z) = \frac{1}{2} \int_{-1}^{1} \left[3\cos^2(\theta_{\text{OH}}) - 1\right] P(\cos(\theta_{\text{OH}})|Z) d\cos(\theta_{\text{OH}}) \tag{9}$$

For Fig. 5e, the probability distribution of the $\cos(\theta_{\text{OH}})$, $P(\cos(\theta_{\text{OH}})|Z)$, was determined for water molecules within a 4-Å bin along the channel axis. To directly compare with the measured NMR orientations, which do not have spatial resolution along the channel axis, we also determined the probability distribution for all water molecules from −12 Å to +12 Å along the channel coordinate.

We also analyzed non-uniformity in the $P(\cos(\theta_{\text{OH}}))$ distribution (Supplementary Fig. 4d) using an entropy parameter ($\Delta\Gamma$) defined as

$$\Delta\Gamma = \sum_{i=0}^{N_{\text{bin}}} P(\cos\theta_{\text{OH}}) \ln[P(\cos\theta_{\text{OH}})] + \ln[N_{\text{bin}}] \tag{10}$$

where N_{bin} is the number of bins used to discretize the $P(\cos(\theta_{\text{OH}}))$ distribution, and the $\ln[N_{\text{bin}}]$ offset is applied such that $\Delta\Gamma = 0$ for a uniform probability distribution. Unlike $\cos(\theta_{\text{OH}})$ and S_{OH}, $\Delta\Gamma$ does not depend on the direction of the reference vector for calculating $\cos(\theta_{\text{OH}})$. Higher $\Delta\Gamma$ values correspond to higher orientational preference. Upon restraining the protein backbone to the solid-state NMR structure, nearly identical anisotropy parameters were observed as in the unrestrained simulations (Supplementary Fig. 4a).

Water–water hydrogen bonding. Water hydrogen bonds were analyzed with the MDAnalysis package[80]. Hydrogen bonds were defined based on default geometric criteria in the package (https://www.mdanalysis.org/docs/documentation_pages/analysis/hbond_analysis.html). Specifically, a water–water hydrogen bond involved a separation of 3.0 Å or less between one water molecule's hydrogen atom and a second water molecule's oxygen atom, and an angle of 120° or more between the oxygen bound to the hydrogen-bonded hydrogen atom, the hydrogen-bonded hydrogen atom, and the acceptor oxygen atom.

A frame stride of 10 was used. The network analysis is carried out for each frame by assigning relevant water molecules in that frame to channel axis slices and then identifying hydrogen bonds across channel-axis slices in that frame. For each frame, each water molecule's channel-axis coordinate for that frame is determined by projecting the water molecule's oxygen atom onto the channel axis. If the water molecule is within the channel-axis coordinate limits of -20–22 Å, and is within 15 Å of the channel-axis vector, it is included in the analysis for that frame. Water molecules are binned in 2-Å-thick bins along the channel axis.

We counted the water–water hydrogen bonds in the simulated trajectories between water molecules assigned to bins separated by 2 Å, in which one water molecule is one slice ($Z = n$) and the second water molecule is in the adjacent slice closer to the C-terminus ($Z = n + 2$; Fig. 7a). For each bin, all hydrogen bonds associated with that bin are those between water molecules in that channel-axis coordinate bin ($Z = n$) and those in the bin 2 Å closer to the C-terminus ($Z = n + 2$). A water–water hydrogen bond is defined as inward, or a donor, when an N-terminal water molecule points its hydrogen atom towards a C-terminal water oxygen atom. A water–water hydrogen bond is defined as outward, or an acceptor, when an N-terminal water oxygen atom receives a hydrogen bond from a C-terminal water hydrogen atom (a C-terminal water molecule points its hydrogen atom towards an N-terminal water oxygen atom, as shown in Fig. 7a). For instance, the hydrogen-bond count associated with the channel-axis coordinate 4.0 Å bin represents the count of hydrogen bonds between the water molecules in the 4.0-Å bin and those in the 6.0-Å bin. The number of outward (acceptor) hydrogen bonds associated with the 4.0-Å coordinate represents the count of hydrogen bonds between water molecules in the 4.0-Å bin and those in the 6.0-Å bin in which the water molecule in the 4.0-Å bin is the acceptor and the water molecule in the 6.0-Å bin is the donor. An inter-slice outward-inward (or acceptor-donor) difference is computed as the difference for each frame for each slice between the inter-slice hydrogen-bond count in which the water molecules in the slice act as acceptors (in water–water hydrogen bonds with the adjacent slice 2 Å closer to the C-terminus) and the inter-slice hydrogen-bond count in which the water molecules in the slice act as donors (in water–water hydrogen bonds with the adjacent slice 2 Å closer to the C-terminus). Bottlenecks are considered to be present in a frame for a slice when there are zero hydrogen bonds between the water molecules in that slice and water molecules in the slice 2.0 Å further toward the C-terminus. For each frame, the total count of inter-slice bottlenecks along the entire channel axis is recorded. Uncertainty is quantified as the standard error of the mean using the averages for the four replicates (as described above) using scipy.stats.sem[81].

Statistics and reproducibility. Sufficient number of scans were used for all NMR experiments to obtain good signal-to-noise. All error bars for NMR analyzed parameters reflect a 68% confidence interval. For MD simulations, the reported values and error bars represent the mean and standard error of the mean, over the four independent trajectories included in calculating the reported quantity.

Reporting summary. Further information on research design is available in the Nature Research Reporting Summary linked to this article.

Data availability
The data that support the findings of this study are available from the corresponding author upon reasonable request. Source data underlying plots shown in figures are provided in Supplementary Data 1.

Code availability
The code and scripts used for the MD portion of this study are available at https://github.com/mjmn/BM2-MD.

References

1. Zhou, Y., Morais-Cabral, J. H., Kaufman, A. & MacKinnon, R. Chemistry of ion coordination and hydration revealed by a K+ channel-Fab complex at 2.0 A resolution. *Nature* **414**, 43–48 (2001).
2. Capponi, S., Heyden, M., Bondar, A.-N., Tobias, D. J. & White, S. H. Anomalous behavior of water inside the SecY translocon. *Proc. Natl Acad. Sci. USA.* **112**, 9016 (2015).
3. Venkatakrishnan, A. J. et al. Diverse GPCRs exhibit conserved water networks for stabilization and activation. *Proc. Natl Acad. Sci. USA* **116**, 3288 (2019).
4. Hummer, G., Rasaiah, J. C. & Noworyta, J. P. Water conduction through the hydrophobic channel of a carbon nanotube. *Nature* **414**, 188–190 (2001).
5. Agmon, N. The grotthuss mechanism. *Chem. Phys. Lett.* **244**, 456–462 (1995).
6. Pomès, R. & Roux, B. Molecular mechanism of H+ conduction in the single-file water chain of the gramicidin channel. *Biophys. J.* **82**, 2304–2316 (2002).
7. Dellago, C., Naor, M. M. & Hummer, G. Proton transport through water-filled carbon nanotubes. *Phys. Rev. Lett.* **90**, 105902 (2003).
8. Tajkhorshid, E. et al. Control of the selectivity of the aquaporin water channel family by global orientational tuning. *Science* **296**, 525 (2002).
9. Kosinska Eriksson, U. et al. Subangstrom resolution X-ray structure details aquaporin-water interactions. *Science* **340**, 1346 (2013).
10. Thomaston, J. L. et al. XFEL structures of the influenza M2 proton channel: Room temperature water networks and insights into proton conduction. *Proc. Natl Acad. Sci. USA* **114**, 13357–13362 (2017).
11. Thomaston, J. L. et al. High-resolution structures of the M2 channel from influenza A virus reveal dynamic pathways for proton stabilization and transduction. *Proc. Natl Acad. Sci. USA* **112**, 14260–14265 (2015).
12. Kovalev, K. et al. Structure and mechanisms of sodium-pumping KR2 rhodopsin. *Sci. Adv.* **5**, eaav2671 (2019).
13. Watkins, L. C., Liang, R., Swanson, J. M. J., DeGrado, W. F. & Voth, G. A. Proton-induced conformational and hydration dynamics in the influenza A M2 channel. *J. Am. Chem. Soc.* **141**, 11667–11676 (2019).
14. Pinto, L. H., Holsinger, L. J. & Lamb, R. A. Influenza virus M2 protein has ion channel activity. *Cell* **69**, 517–528 (1992).
15. Hong, M., Fritzsching, K. J. & Williams, J. K. Hydrogen-bonding partner of the proton-conducting histidine in the influenza M2 proton channel revealed from 1H chemical shifts. *J. Am. Chem. Soc.* **134**, 14753–14755 (2012).
16. Wang, C., Lamb, R. A. & Pinto, L. H. Activation of the M2 ion channel of influenza virus: a role for the transmembrane domain histidine residue. *Biophys. J.* **69**, 1363–1371 (1995).
17. Hu, F., Luo, W. & Hong, M. Mechanisms of proton conduction and gating in influenza M2 proton channels from solid-state NMR. *Science* **330**, 505–508 (2010).
18. Hu, F., Schmidt-Rohr, K. & Hong, M. NMR detection of pH-dependent histidine-water proton exchange reveals the conduction mechanism of a transmembrane proton channel. *J. Am. Chem. Soc.* **134**, 3703–3713 (2012).
19. Tang, Y. J., Zaitseva, F., Lamb, R. A. & Pinto, L. H. The gate of the influenza virus M-2 proton channel is formed by a single tryptophan residue. *J. Biol. Chem.* **277**, 39880–39886 (2002).
20. Mandala, V. S., Liao, S. Y., Kwon, B. & Hong, M. Structural basis for asymmetric conductance of the influenza M2 proton channel investigated by solid-state NMR spectroscopy. *J. Mol. Biol.* **429**, 2192–2210 (2017).
21. Liang, R., Li, H., Swanson, J. M. J. & Voth, G. A. Multiscale simulation reveals a multifaceted mechanism of proton permeation through the influenza A M2 proton channel. *Proc. Natl Acad. Sci. USA* **111**, 9396 (2014).
22. Hu, J. et al. Histidines, heart of the hydrogen ion channel from influenza A virus: toward an understanding of conductance and proton selectivity. *Proc. Natl Acad. Sci. USA* **103**, 6865–6870 (2006).
23. Liao, S. Y., Yang, Y., Tietze, D. & Hong, M. The influenza m2 cytoplasmic tail changes the proton-exchange equilibria and the backbone conformation of the transmembrane histidine residue to facilitate proton conduction. *J. Am. Chem. Soc.* **137**, 6067–6077 (2015).
24. Acharya, A. et al. Structural mechanism of proton transport through the influenza A M2 protein. *Proc. Natl Acad. Sci. USA* **107**, 15075–15080 (2010).
25. Mandala, V. S., Gelenter, M. D. & Hong, M. Transport-relevant protein conformational dynamics and water dynamics on multiple time scales in an archetypal proton channel: insights from solid-state NMR. *J. Am. Chem. Soc.* **140**, 1514–1524 (2018).
26. Williams, J. K. & Hong, M. Probing membrane protein structure using water polarization transfer solid-state NMR. *J. Magn. Reson.* **247**, 118–127 (2014).
27. Mandala, V. S., Loftis, A. R., Shcherbakov, A. A., Pentelute, B. L. & Hong, M. Atomic structures of closed and open influenza B M2 proton channel reveal the conduction mechanism. *Nat. Struct. Mol. Biol.* **27**, 160–167 (2020).
28. Kwon, B., Roos, M., Mandala, V. S., Shcherbakov, A. A. & Hong, M. Elucidating relayed proton transfer through a his-trp-his triad of a transmembrane proton channel by solid-state NMR. *J. Mol. Biol.* **431**, 2554–2566 (2019).
29. Williams, J. K., Shcherbakov, A. A., Wang, J. & Hong, M. Protonation equilibria and pore-opening structure of the dual-histidine influenza B virus M2 transmembrane proton channel from solid-state NMR. *J. Biol. Chem.* **292**, 17876–17884 (2017).
30. Williams, J. K. et al. Investigation of the conformation, proton conduction, and hydration of the influenza B virus M2 transmembrane proton channel. *J. Am. Chem. Soc.* **138**, 8143–8155 (2016).
31. Van Melckebeke, H. et al. Atomic-resolution three-dimensional structure of HET-s(218–289) amyloid fibrils by solid-state NMR spectroscopy. *J. Am. Chem. Soc.* **132**, 13765–13775 (2010).

32. Sehgal, A. A., Duma, L., Bodenhausen, G. & Pelupessy, P. Fast proton exchange in histidine: measurement of rate constants through indirect detection by NMR spectroscopy. *Chem. Eur. J.* **20**, 6332–6338 (2014).

33. Kateb, F., Pelupessy, P. & Bodenhausen, G. Measuring fast hydrogen exchange rates by NMR spectroscopy. *J. Magn. Reson.* **184**, 108–113 (2007).

34. Liepinsh, E., Otting, G. & Wüthrich, K. NMR spectroscopy of hydroxyl protons in aqueous solutions of peptides and proteins. *J. Biomol. NMR* **2**, 447–465 (1992).

35. Skelton, N. J., Kördel, J., Akke, M. & Chazin, W. J. Nuclear magnetic resonance studies of the internal dynamics in apo, (Cd2+)1 and (Ca2+)2 Calbindin D9k: The rates of amide proton exchange with solvent. *J. Mol. Biol.* **227**, 1100–1117 (1992).

36. Luo, W. & Hong, M. Conformational changes of an ion channel detected through water−protein interactions using solid-state NMR spectroscopy. *J. Am. Chem. Soc.* **132**, 2378–2384 (2010).

37. Ader, C. et al. Structural rearrangements of membrane proteins probed by water-edited solid-state NMR spectroscopy. *J. Am. Chem. Soc.* **131**, 170–176 (2009).

38. Bloembergen, N., Purcell, E. M. & Pound, R. V. Relaxation effects in nuclear magnetic resonance absorption. *Phys. Rev.* **73**, 679–712 (1948).

39. Ropp, J., Lawrence, C., Farrar, T. C. & Skinner, J. L. Rotational motion in liquid water is anisotropic: a nuclear magnetic resonance and molecular dynamics simulation study. *J. Am. Chem. Soc.* **123**, 8047–8052 (2001).

40. Rovó, P. et al. Mechanistic insights into microsecond time-scale motion of solid proteins using complementary 15N and 1H relaxation dispersion techniques. *J. Am. Chem. Soc.* **141**, 858–869 (2019).

41. Trott, O. & Palmer, A. G. R1ρ relaxation outside of the fast-exchange limit. *J. Magn. Reson.* **154**, 157–160 (2002).

42. Palmer, A. G. & Massi, F. Characterization of the dynamics of biomacromolecules using rotating-frame spin relaxation NMR spectroscopy. *Chem. Rev.* **106**, 1700–1719 (2006).

43. Nucci, N. V., Pometun, M. S. & Wand, A. J. Site-resolved measurement of water-protein interactions by solution NMR. *Nat. Struct. Mol. Biol.* **18**, 245–249 (2011).

44. Gun'ko, V. M. & Turov, V. V. Structure of hydrogen bonds and 1H NMR spectra of water at the interface of oxides. *Langmuir* **15**, 6405–6415 (1999).

45. Schanda, P. & Ernst, M. Studying dynamics by magic-angle spinning solid-state NMR spectroscopy: principles and applications to biomolecules. *Prog. Nucl. Magn. Reson. Spectrosc.* **96**, 1–46 (2016).

46. Smith, A. A., Ernst, M. & Meier, B. H. Because the light is better here: correlation-time analysis by NMR spectroscopy. *Angew. Chem. Int. Ed.* **56**, 13590–13595 (2017).

47. Teixeira, J., Zanotti, J. M., Bellissent-Funel, M. C. & Chen, S. H. Water in confined geometries. *Phys. B Condens. Matter* **234–236**, 370–374 (1997).

48. Bellissent-Funel, M. C. Structure of confined water. *J. Phys. Condens. Matter* **13**, 9165–9177 (2001).

49. Tuckerman, M., Laasonen, K., Sprik, M. & Parrinello, M. Ab initio molecular dynamics simulation of the solvation and transport of hydronium and hydroxyl ions in water. *J. Chem. Phys.* **103**, 150–161 (1995).

50. Hong, M. et al. Coupling amplification in 2D MAS NMR and its application to torsion angle determination in peptides. *J. Magn. Reson.* **129**, 85–92 (1997).

51. Duma, L., Abergel, D., Tekely, P. & Bodenhausen, G. Proton chemical shift anisotropy measurements of hydrogen-bonded functional groups by fast magic-angle spinning solid-state NMR spectroscopy. *Chem. Commun.* **20**, 2361–2363 (2008).

52. Marion, D., Gauto, D. F., Ayala, I., Giandoreggio-Barranco, K. & Schanda, P. Microsecond protein dynamics from combined Bloch-McConnell and Near-Rotary-Resonance R(1p) relaxation-dispersion MAS NMR. *Chemphyschem* **20**, 276–284 (2019).

53. Modig, K. & Halle, B. Proton magnetic shielding tensor in liquid water. *J. Am. Chem. Soc.* **124**, 12031–12041 (2002).

54. Keeler, E. G., Fritzsching, K. J. & McDermott, A. E. Refocusing CSA during magic angle spinning rotating-frame relaxation experiments. *J. Magn. Reson.* **296**, 130–137 (2018).

55. Hong, M., Schmidt-Rohr, K. & Pines, A. Measurement of signs and magnitudes of C-H dipolar couplings in lecithin. *J. Am. Chem. Soc.* **117**, 3310–3311 (1995).

56. Hong, M., Schmidt-Rohr, K. & Zimmermann, H. Conformational constraints on the headgroup and sn-2 chain of bilayer DMPC from NMR dipoalr couplings. *Biochemistry* **35**, 8335–8341 (1996).

57. Khurana, E. et al. Molecular dynamics calculations suggest a conduction mechanism for the M2 proton channel from influenza A virus. *Proc. Natl Acad. Sci. USA* **106**, 1069–1074 (2009).

58. Ghosh, A., Qiu, J., DeGrado, W. F. & Hochstrasser, R. M. Tidal surge in the M2 proton channel, sensed by 2D IR spectroscopy. *Proc. Natl Acad. Sci. USA* **108**, 6115 (2011).

59. Zhang, Y., Zhang, H. & Zheng, Q. A unique activation–promotion mechanism of the influenza B M2 proton channel uncovered by multiscale simulations. *Phys. Chem. Chem. Phys.* **21**, 2984–2991 (2019).

60. Zhang, Y. & Zheng, Q.-C. What are the effects of the serine triad on proton conduction of an influenza B M2 channel? An investigation by molecular dynamics simulations. *Phys. Chem. Chem. Phys.* **21**, 8820–8826 (2019).

61. Laage, D. & Hynes, J. T. A molecular jump mechanism of water reorientation. *Science* **311**, 832–835 (2006).

62. Hassanali, A., Giberti, F., Cuny, J., Kühne, T. D. & Parrinello, M. Proton transfer through the water gossamer. *Proc. Natl Acad. Sci. USA* **110**, 13723–13728 (2013).

63. Watanabe, S., Imai, M., Ohara, Y. & Odagiri, T. Influenza B virus BM2 protein is transported through the trans-golgi network as an integral membrane protein. *J. Virol.* **77**, 10630–10637 (2003).

64. Bernard, G. M. et al. Methylammonium lead chloride: a sensitive sample for an accurate NMR thermometer. *J. Magn. Reson.* **283**, 14–21 (2017).

65. Bennett, A. E., Rienstra, C. M., Auger, M., Lakshmi, K. V. & Griffin, R. G. Heteronuclear decoupling in rotating solids. *J. Chem. Phys.* **103**, 6951–6958 (1995).

66. Harris, R. K. et al. Further conventions for NMR shielding and chemical shifts (IUPAC recommendations 2008). *Pure Appl. Chem.* **80**, 59–84 (2008).

67. Veshtort, M. & Griffin, R. G. SPINEVOLUTION: a powerful tool for the simulation of solid and liquid state NMR experiments. *J. Magn. Reson.* **178**, 248–282 (2006).

68. Wales, D. J. & Hodges, M. P. Global minima of water clusters (H2O)n, n≤21, described by an empirical potential. *Chem. Phys. Lett.* **286**, 65–72 (1998).

69. McNeill, S. A., Gor'kov, P. L., Shetty, K., Brey, W. W. & Long, J. R. A low-E magic angle spinning probe for biological solid state NMR at 750MHz. *J. Magn. Reson.* **197**, 135–144 (2009).

70. Jo, S., Kim, T., Iyer, V. G. & Im, W. CHARMM-GUI: a web-based graphical user interface for CHARMM. *J. Comput. Chem.* **29**, 1859–1865 (2008).

71. Zhang, L. & Hermans, J. Hydrophilicity of cavities in proteins. *Proteins* **24**, 433–438 (1996).

72. Parrinello, M. & Rahman, A. Polymorphic transitions in single crystals: a new molecular dynamics method. *J. Appl. Phys.* **52**, 7182–7190 (1981).

73. Parrinello, M. & Rahman, A. Crystal structure and pair potentials: a molecular-dynamics study. *Phys. Rev. Lett.* **45**, 1196–1199 (1980).

74. Bussi, G., Donadio, D. & Parrinello, M. Canonical sampling through velocity rescaling. *J. Chem. Phys.* **126**, 014101 (2007).

75. Berendsen, H. J. C., van der Spoel, D. & van Drunen, R. GROMACS: A message-passing parallel molecular dynamics implementation. *Comput. Phys. Commun.* **91**, 43–56 (1995).

76. Hess, B., Bekker, H., Berendsen, H. J. C. & Fraaije, J. G. E. M. LINCS: a linear constraint solver for molecular simulations. *J. Comput. Chem.* **18**, 1463–1472 (1997).

77. Pang, Y.-P. Low-mass molecular dynamics simulation: a simple and generic technique to enhance configurational sampling. *Biochem. Biophys. Res. Commun.* **452**, 588–592 (2014).

78. Best, R. B. & Mittal, J. Free-energy landscape of the GB1 hairpin in all-atom explicit solvent simulations with different force fields: similarities and differences. *Proteins* **79**, 1318–1328 (2011).

79. Jorgensen, W. L. & Jenson, C. Temperature dependence of TIP3P, SPC, and TIP4P water from NPT Monte Carlo simulations: seeking temperatures of maximum density. *J. Comput. Chem.* **19**, 1179–1186 (1998).

80. Michaud-Agrawal, N., Denning, E. J., Woolf, T. B. & Beckstein, O. MDAnalysis: a toolkit for the analysis of molecular dynamics simulations. *J. Comput. Chem.* **32**, 2319–2327 (2011).

81. Virtanen, P. et al. SciPy 1.0: fundamental algorithms for scientific computing in Python. *Nat. Methods* **17**, 261–272 (2020).

Acknowledgements

Author contributions

M.H. designed the project. M.D.G., V.S.M., and A.J.D conducted the solid-state NMR experiments, analyses, and NMR numerical simulations. M.J.M.N., D.A.S. and A.P. W. performed the MD simulations and analyses. All authors discussed and interpreted the data and wrote the manuscript.

Competing interests

The authors declare no competing interests.

Additional information

Supplementary information The online version contains supplementary material available at https://doi.org/10.1038/s42003-021-01847-2.

Correspondence and requests for materials should be addressed to M.H.

Reprints and permission information is available at http://www.nature.com/reprints

Publisher's note Springer Nature remains neutral with regard to jurisdictional claims in published maps and institutional affiliations.

Supplementary Information

Water Orientation and Dynamics in the Closed and Open Influenza B Virus M2 Proton Channels

Martin D. Gelenter[$], Venkata S. Mandala[$], Michiel J.M. Niesen[$], Dina A. Sharon[$], Aurelio J. Dregni, Adam P. Willard, and Mei Hong*

Department of Chemistry, Massachusetts Institute of Technology, 77 Massachusetts Avenue, Cambridge, MA 02139

[$] These authors contributed equally
* Corresponding author: Mei Hong: meihong@mit.edu

Supplementary Methods
Water-protein spin diffusion data analysis
      Here we derive the analytical equations for the square-root time dependence of the buildup intensities of water transfer to protein. We also prove how the relative intensities of the initial-regime water transferred intensities reflect the relative amounts of water.

      Spin diffusion from a one-dimensional point source can be described analytically[1] as:

$$M(x,t) = \frac{W}{\sqrt{\pi Dt}} \exp\left(\frac{-(x-x_S)^2}{4Dt}\right) \tag{1}$$

where M is the magnetization at position x and time t, x_S is the position of the point source, W is the amount of water contributing to diffusion, and D is the effective spin diffusion coefficient for magnetization transfer between water and protein, which has contributions from both chemical exchange and spin diffusion [2]. We assume that the spin diffusion coefficients of water in the high- and low-pH channels is approximately the same and is much greater than the effective diffusion coefficient D. Since proton chemical exchange is faster at pH 7.5 than at pH 4.5 [3-5], $D_{pH7.5}$ is greater than or equal to $D_{pH4.5}$. Thus W is the quantity of interest for the water-count experiments. In our samples, magnetization transfer originates from a continuum of water molecules at different positions to protein. This modifies the diffusion equation to:

$$M_{dom}(x,t) = \int_{-\infty}^{0} \frac{W}{\sqrt{\pi Dt}} \exp\left(\frac{-(x-x_S)^2}{4Dt}\right) dx = W\, \mathrm{erfc}\left(\frac{x}{\sqrt{4Dt}}\right) \tag{2}$$

where erfc is the error function. Now we derive the magnetization transferred from the water slab to our protein, assuming the protein has a fixed width a from the edge of the water source :

$$M_{prot}(t) = \int_0^a W\, \mathrm{erfc}\left(\frac{x}{\sqrt{4Dt}}\right) dx = \frac{2W\sqrt{Dt}}{\sqrt{\pi}}\left[1-\exp\left(\frac{-a^2}{4Dt}\right)\right] + aW\, \mathrm{erfc}\left(\frac{a}{2\sqrt{Dt}}\right) \tag{3}$$

      The above equation can be simplified using the parameter $b = \dfrac{a}{2\sqrt{Dt}}$:

$$M_{prot}(t) = 2W\sqrt{Dt}\left[\frac{1}{\sqrt{\pi}}\left(1-e^{-b^2}\right) + 2b\, \mathrm{erfc}(b)\right] \tag{4}$$

      At short mixing times where $2\sqrt{Dt} \ll a$, $b \to \infty$, thus equation (4) reduces to:

$$M_{prot}(t \to 0) \approx \frac{2W}{\sqrt{\pi}}\sqrt{Dt} \tag{5}$$

Thus, the initial-regime water-transferred magnetization is directly proportional to the water density W. At long mixing times where $2\sqrt{Dt} \gg a$, $b \to 0$, and equation (4) reduces to:

$$M_{prot}(t \to \infty) \approx \frac{2W}{\sqrt{\pi}}\sqrt{Dt}b = \frac{Wa}{\sqrt{\pi}} \qquad (6)$$

The intensity ratio S/S_0 between short and long mixing times is thus inversely related to the protein-water distance a:

$$\frac{S}{S_0} = \frac{M_{prot}(t \to 0)}{M_{prot}(t \to \infty)} \approx \frac{2\sqrt{Dt}}{a} \qquad (7)$$

In addition, the water-transferred magnetization in the initial regime (eq. 5) is proportional to the amount of water, W, and the square root of the effective spin diffusion coefficient D. This means that the ratio of the initial-regime spectral intensities between the two samples reports the ratio of the products of the amount of water and the square root of the effective diffusion coefficient in the low-pH and high-pH channels. Since D is larger at high pH than low pH, the ratio of the initial-regime intensities represents an upper bound to the relative amount of water:

$$\frac{S_{pH4.5}}{S_{pH7.5}} \approx \sqrt{\frac{D_{pH4.5}}{D_{pH7.5}}}\frac{W_{pH4.5}}{W_{pH7.5}} \geq \frac{W_{pH4.5}}{W_{pH7.5}} \qquad (8)$$

Water $T_2{'}$ and $R_{1\rho}$ relaxation analysis

While the BPP theory can be applied readily to analysis of rapidly tumbling molecules in solution, accurate extraction of τ_{rot} in semi-solids is affected by coherent effects [6]. The longer τ_{rot} compared to bulk-like water correlation times (**Table S1**) indicates that the channel-bound water motion is highly restricted. The slower $T_2{'}$ rates at low pH indicates that the channel water is more mobile in the low-pH channel on the nanosecond timescale.

The ^{1}H $R_{1\rho}$ relaxation dispersion profiles (**Fig. 3d**) can be described by the Bloch-McConnell formalism[7] to extract the kinetic parameters of exchange. The low-pH sample shows lower $R_{1\rho}$ values for channel-bound water at both low and high spin-lock fields (**Fig. 3d**). Fitting the dispersion data to a two-state exchange model (**Table S2**) yielded an $R_{1\rho}^0$ of 76±5 s^{-1} at high-pH and 39±4 s^{-1} at low-pH, and an exchange time τ_{ex} of 9.5±0.9 μs at high-pH and 5.2±0.3 μs at low-pH. For both samples, we obtain $\phi_{ex} = p_1 p_2 \Delta\omega^2 \sim 20\cdot10^6$ rad^2 s^{-2}, where p_1 and p_2 are the population fractions of the two states and $\Delta\omega$ is the isotropic shift difference between the two states. This chemical shift difference can be between protein-bound and protein-unbound water in the channel, or between bound water protons and labile protein protons. However, the exchange rates of $1/\tau_{ex} \sim 10^5$ s^{-1} are faster than the exchange rates of all labile OH and NH protons, except for histidine at ~273 K [8]. If the two populations are each ~50%, the ϕ_{ex} values indicate a chemical shift difference of ~1.4 kHz for the high-pH channel water and ~1.6 kHz for low-pH channel water. Conversely, if we assume the rarer state is 1% populated, then the ϕ_{ex} values indicate chemical shift differences of ~7 kHz for the high-pH sample and ~8 kHz for the low-pH sample. This ~10

ppm difference would be consistent with exchange between a water proton and a histidine sidechain proton, and the k_{ex} of 5.2±0.3 µs at low pH is consistent with the expected exchange rate between histidine and water at pH 4.5 [3], however at pH 7.5 we expect an exchange rate of 100,000 s^{-1} or more [9], which is an order of magnitude faster than the observed k_{ex} at pH 7.5. Therefore, based on the exchange rates fit to the $R_{1\rho}$ relaxation dispersion curves, we do not attribute the dispersion to exchange between histidine and water, but rather attribute it to exchange between two water populations. It is unlikely for the two pools of water that undergo fast exchanging to have large shift differences of ~10 ppm (which is ~8 kHz on the 800 MHz spectrometer). Therefore we assume the two states are both significantly populated and chemical shift differences of ~2 ppm. This chemical shift difference is much smaller than the exchange rate, which is consistent with the observation of a single water ^1H peak in the spectrum. Although 2 ppm is a large difference for two exchanging water populations, this isotropic chemical shift difference is similar to the 1.1 ppm difference between buried and hydration water interacting with ubiquitin encapsulated within a reverse micelle [10] and the 2.6 ppm difference in chemical shifts of water adsorbed to silica and alumina oxides [11].

In contrast to the ^{13}C-detected experiments, the ^1H-detected $R_{1\rho}$ experiments with a 40 ms T_2' filter to select for bulk-like water show no relaxation dispersion (**Fig. S3e**) and much slower $R_{1\rho}^0$ of 5.3±1.9 s^{-1} at high pH and 5.6±0.7 s^{-1} at low pH. When the ^1H-detected $R_{1\rho}$ experiments were conducted without a T_2' filter, which capture both bulk-like and lipid-bound water, then we observed a small dispersion that is similar for the high- and low-pH samples (**Fig. S3e**). The $R_{1\rho}^0$ values are 23±3 s^{-1} at high pH and 20±5 s^{-1} at low pH, while the τ_{ex} times are 3.6±0.8 µs at high pH and 3.0±0.9 µs at low pH. Precise interpretation of these microsecond exchange processes is complicated by the presence of coherent contributions under MAS, which can bias the extracted exchange parameters[6,12,13]. Nevertheless, the 2-10 fold faster $R_{1\rho}^0$ in the ^{13}C-detected experiments compared to the ^1H-detected experiments indicates that the motion of channel-bound water is significantly anisotropic. Moreover, the slower intrinsic relaxation rate and shorter exchange time constant for the low-pH sample indicate that the channel-bound water is more dynamic on the microsecond timescale in the open channel than in the closed channel.

Supplementary Table 1. ^{1}H-detected and ^{13}C-detected water ^{1}H $T_2{}'$ relaxation times and the resulting rotational correlation times τ_{rot} calculated using the BPP theory [14].

Sample	Detection nucleus	Water Pool	$T_2{}'$	τ_{rot}
pH 7.5	^{1}H	Bulk-like	39.4±1.2 ms	0.68 ns
	^{1}H	Lipid	1.5±0.2 ms	20 ns
	^{13}C	Channel	4.0±0.1 ms	7.6 ns
pH 4.5	^{1}H	Bulk-like	47.7±2.2 ms	0.52 ns
	^{1}H	Lipid	2.2±0.3 ms	14 ns
	^{13}C	Channel	5.5±0.1 ms	5.6 ns

Supplementary Table 2. ^{1}H-detected and ^{13}C-detected water ^{1}H $R_{1\rho}$ relaxation dispersion fits assuming a two-state exchange process.
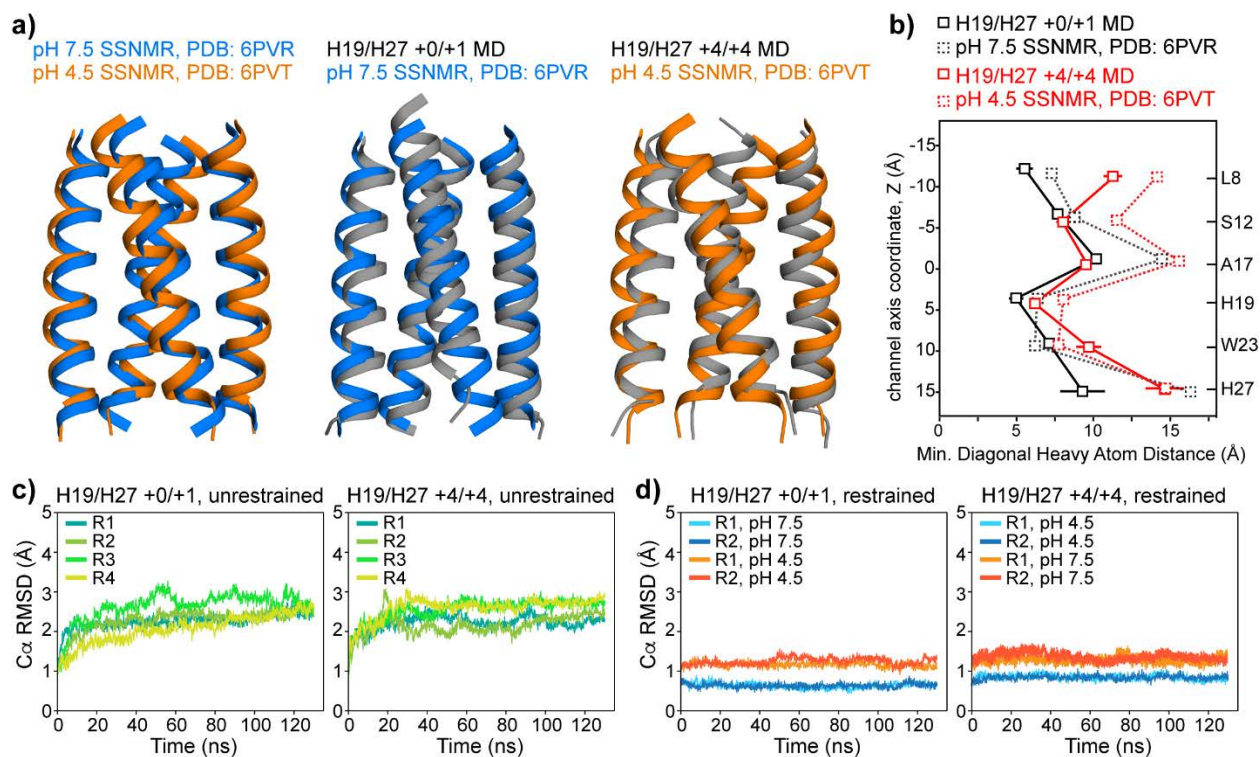
Sample	Detection nucleus	$T_2{}'$ filter	Water Pool	$R_{1\rho}{}^0$	τ_{ex}	τ_{ex} (10^6 rad^{2}s^{-2})
pH 7.5	^{1}H	None	Bulk-like and Lipid	23±3 s^{-1}	3.6±0.8 µs	5±2
	^{1}H	40 ms	Bulk-like	5.3±1.9 s^{-1}	–	–
	^{13}C	None	Channel	76±5 s^{-1}	9.5±0.9 µs	19±2
pH 4.5	^{1}H	None	Bulk-like and Lipid	20±5 s^{-1}	3.0±0.9 µs	6±3
	^{1}H	40 ms	Bulk-like	5.6±0.7 s^{-1}	–	–
	^{13}C	None	Channel	39±4 s^{-1}	5.2±0.3 µs	26±2

Supplementary Table 3. Energy minimization and equilibration protocol and accompanying force constants with units of kJ mol^{-1} nm^{-2}.

Duration	Ensemble	BB restraint	SC restraint	LH restraint	LT restraint
5000 steps	EM	4000	2000	1000	1000
25 ps	NVT	4000	2000	1000	1000
25 ps	NVT	2000	1000	1000	400
25 ps	NPT	1000	500	400	200
100 ps	NPT	500	200	200	200
100 ps	NPT	200	50	40	100
100 ps	NPT	50	0	0	0
30 ns	NPT	0 or 50 (see methods)	0	0	0

Supplementary Table 4. Average channel-axis coordinates for Cα atom of residues I7 to H27, taken over the four independent unrestrained 100 ns MD simulations of the closed BM2 channel (+0/+1 H19/H27 charge state) and the open channel (+4/+4 H19/H27 charge state) at 277K, respectively.

| Residue	$\langle Z \rangle_{closed}$ (Å)	$\langle Z \rangle_{open}$ (Å)
I7	-14	-13.5
L8	-12.2	-11.2
S9	-11.5	-10.9
I10	-10.1	-9.9
C11	-8.0	-7.4
S12	-6.7	-6.0
F13	-5.8	-5.6
I14	-3.9	-3.8
L15	-2.1	-1.6
S16	-1.2	-0.7
A17	0	0
L18	2.2	2.2
H19	3.6	4.0
F20	4.3	4.6
M21	6.0	5.8
A22	8.1	8.1
W23	9.1	9.4
T24	10.0	10.0
I25	11.8	11.9
G26	13.4	13.8
H27	14.8	14.7

Supplementary Figure 1. Comparison of the MD and solid-state NMR structures of BM2 and the time evolution of MD trajectories. (**a**) (*left*) Overlay of the lowest energy state from the pH 7.5 (blue, PDB ID 6PVR) and pH 4.5 (orange, PDB ID 6PVT) solid-state NMR structural ensembles. (*right*) Overlays of the backbone traces of the MD equilibrated structures (grey) and the solid-state NMR experimental structures (red). (**b**) Minimum diagonal heavy-atom distances, a proxy for the pore radius, as a function of the channel-axis coordinate. The calculation was carried out for L8, S12, S16, H19, W23, and H27. There is good agreement between the MD equilibrated structures and the experimental solid-state NMR structures. (**c**) Time-evolution of Cα RMSD with respect to the solid-state NMR structures in the unrestrained MD trajectories. The four replicates (R1-R4) are shown in different shades of green. (**d**) Time-evolution of Cα RMSD with respect to the solid-state NMR structures in the restrained MD trajectories. The H19/H27 +0/+1 and +4/+4 MD states were restrained either to the pH 7.5 (PDB ID 6PVR) or the pH 4.5 (PDB ID 6PVT) solid-state NMR structures for two replicates. These restrained simulations show average Cα RMSDs below 1.50 Å.
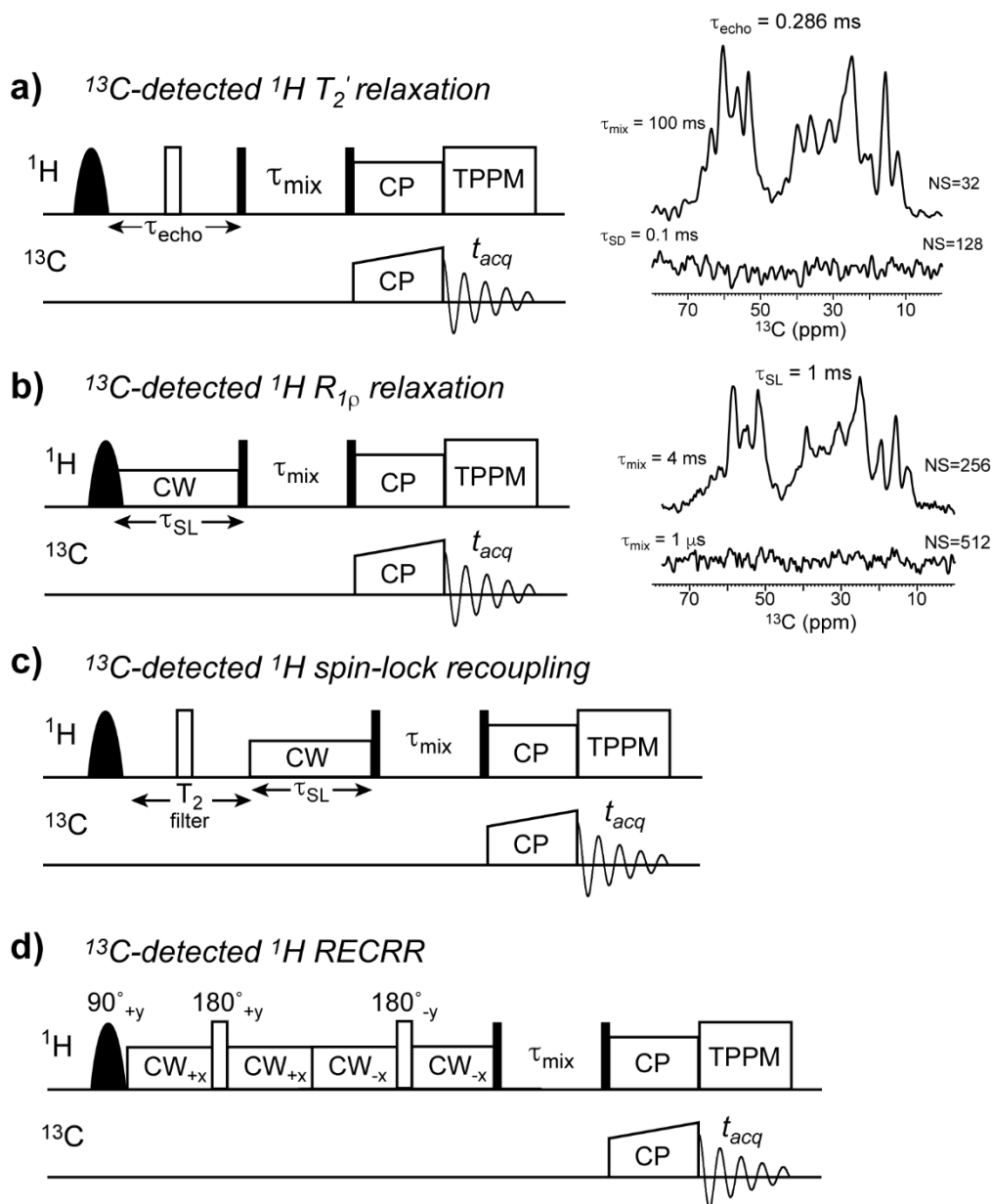
Supplementary Figure 2. Pulse sequences for the solid-state NMR experiments to detect water dynamics. (**a**) ^{13}C-detected ^{1}H T_2' experiment begins with a selective ^{1}H excitation pulse, followed by a variable T_2 filter period, a spin diffusion period τ_{mix}, and cross-polarization (CP) to transfer water ^{1}H polarization to protein ^{13}C for detection. Shown on the right is a pair of control spectra measured with a τ_{echo} period of 0.286 ms and with τ_{mix} of 100 ms and 0.1 ms. The 0.1 ms spectrum has no signal intensity, indicating that all protein ^{1}H magnetization is suppressed by the selective echo and a 0.286 ms echo period. Shown on the right is a pair of control spectra measured with 1 ms τ_{SL} and τ_{mix} times of 4 ms and 1 μs. The null intensities in the 1 μs spectrum indicate that all protein ^{1}H magnetization is suppressed. (**c**) ^{13}C-detected ^{1}H $R_{1\rho}$ spin-lock recoupling experiment. A ^{1}H T_2' filter precedes the spin-lock recoupling pulse to remove the magnetization of rigid protons. (**d**) ^{13}C-detected ^{1}H RECRR experiment.
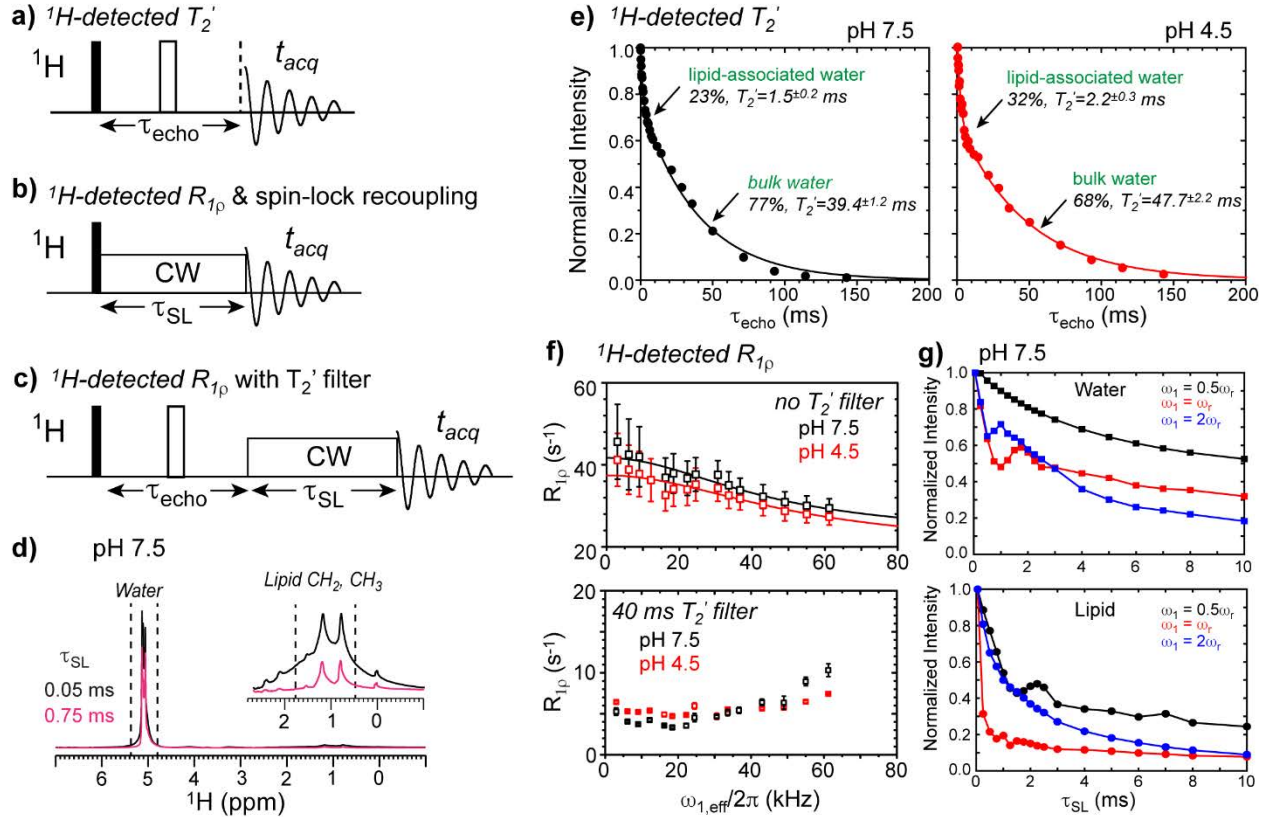
Supplementary Figure 3. ^{1}H-detected T_2' relaxation, $R_{1\rho}$ relaxation, and spin-lock recoupling of water in membrane-bound BM2 samples. All spectra were measured at a sample temperature of ~273 K. (**a**) Pulse sequence for measuring ^{1}H T_2'. (**b**) Pulse sequence for measuring ^{1}H $R_{1\rho}$ and for ^{1}H spin-lock recoupling. (**c**) Pulse sequence for measuring ^{1}H $R_{1\rho}$ that utilizes a T_2' filter to select for mobile, isotropic water. (**d**) Representative ^{1}H spectra at two spin-lock times for the pH 7.5 sample. The integration areas for the water peak and the lipid chain ^{1}H signals are indicated with dashed lines. (**e**) ^{1}H-detected water apparent transverse relaxation decays at pH 7.5 and pH 4.5. Both decays are biexponential. The small component of fast initial decay results from lipid-associated water while the major component of slow decay results from bulk-like water. The populations and T_2' values are indicated. (**f**) ^{1}H-detected on-resonance $R_{1\rho}$ relaxation dispersion curves as a function of spin-lock field strength. (*top*) The pH 7.5 (*black*) and pH 4.5 (*red*) samples both exhibit relaxation dispersion. (*bottom*) Addition of a 40 ms ^{1}H T_2' filter before the spin-lock period to suppress the lipid-associated water removed the relaxation dispersion, indicating that lipid-associated water is responsible for the dispersion. (**g**) ^{1}H-detected spin-lock recoupling data for all water protons and for lipid chain protons in the high-pH BM2 sample. The curves were measured at ω_1 values of $0.5\omega_r$, ω_r, and $2\omega_r$. The water signal, which results from bulk-like, lipid-associated and channel water, shows oscillations at $\omega_1 = \omega_r$ and $2\omega_r$ but not at $\omega_1 = 0.5\omega_r$, indicating CSA recoupling. The minima of the oscillations are higher than the minima of channel-bound water (**Fig. 5a**), indicating that only a fraction of all water is anisotropic. The lipid protons (bottom panel) show oscillations at $\omega_1 = 0.5\omega_r$ and ω_r but little oscillation at $\omega_1 = 2\omega_r$, indicating that ^{1}H-^{1}H dipolar interaction is recoupled.
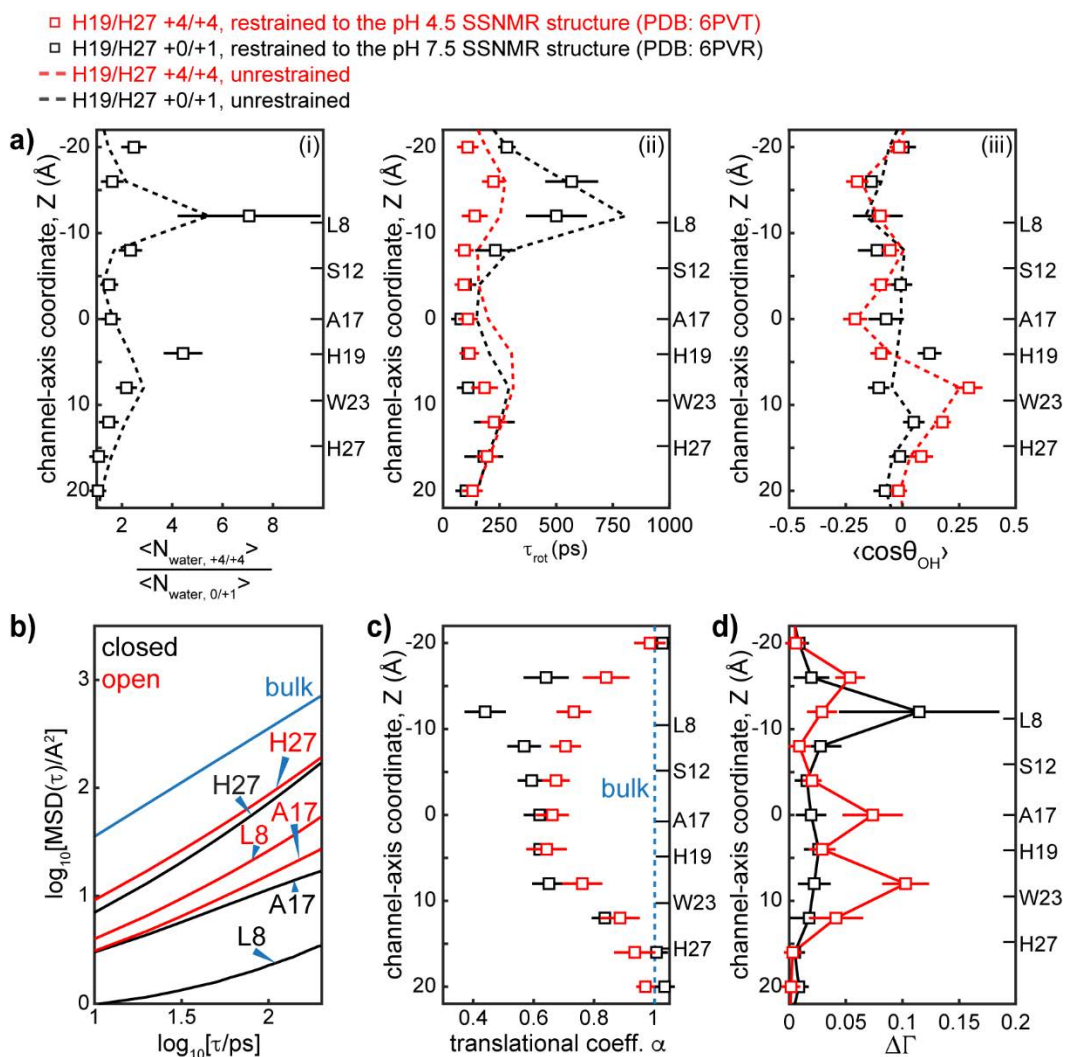
Supplementary Figure 4. (**a**) Comparison of unrestrained and restrained MD simulations of channel water dynamics. Simulations for channels whose backbone has been restrained to the solid-state NMR structures are shown as squares while unrestrained simulations are shown as dashed lines. Results are insensitive to the use of position restraints. Shown are: (**i**) the ratio of the water counts between the open and closed BM2 channels, (**ii**) the rotational correlation time, τ_{rot}, and (**iii**) time-averaged $\cos\theta_{OH}$ of channel water. (**b**) Mean-squared displacement of water as a function of time near various pore-lining residues for the closed (*black*) and open (*red*) channels. Bulk-like water diffusion is plotted as a blue line for comparison. Diffusion is faster in the open, H19/H27 +4/+4 channel on average. In both the open$^{+4/+4}$ channel and the closed$^{0/+1}$ channel, diffusion is the fastest near H27 (Z=20). In the closed$^{0/+1}$ state, diffusion is especially slow near L8 (Z=-12). (**c**) Translational diffusion power-law exponent α along the channel axis. All α values inside the channel are below 1, indicating sub-diffusive behavior. (**d**) Entropy of the $P(\cos(\theta_{OH}))$ distribution, which reports water orientations independent of the reference vector direction. A higher value means more ordered water. The open channel has a larger proportion of ordered water than the closed channel.
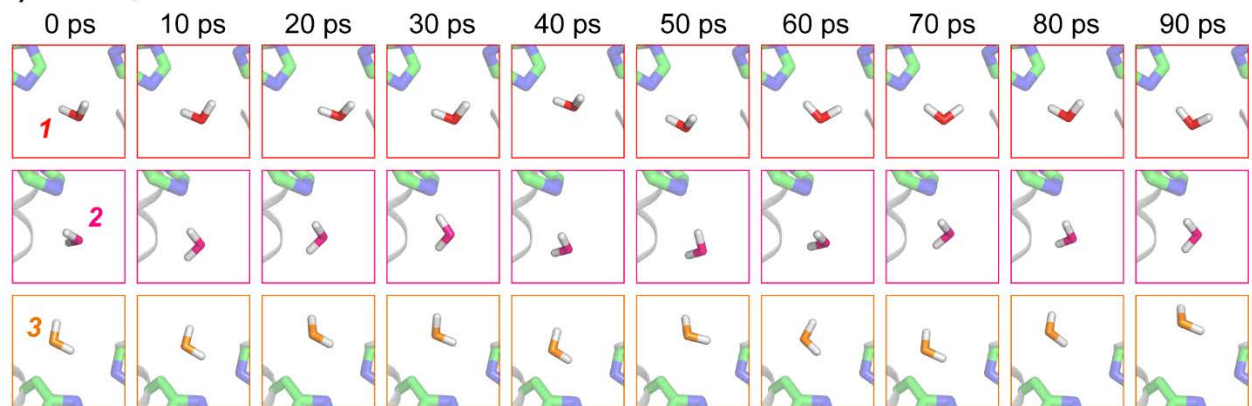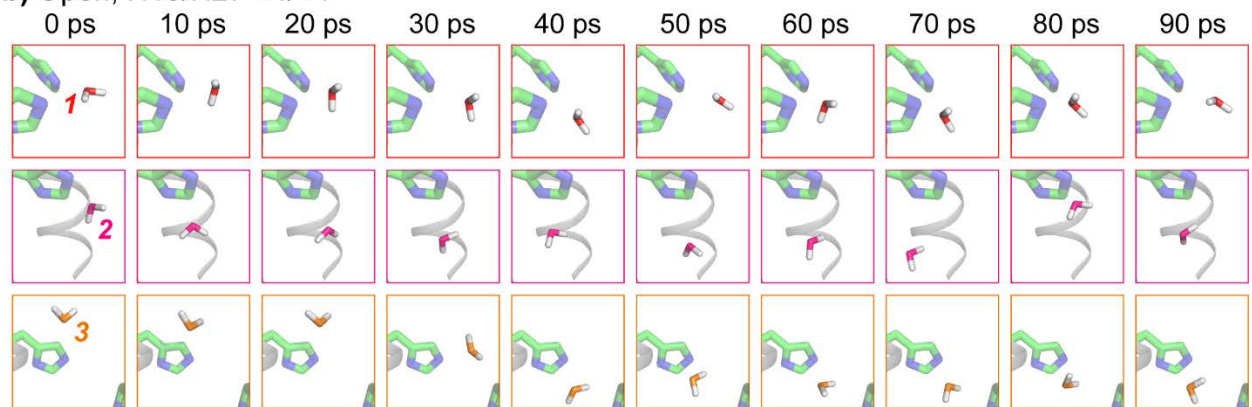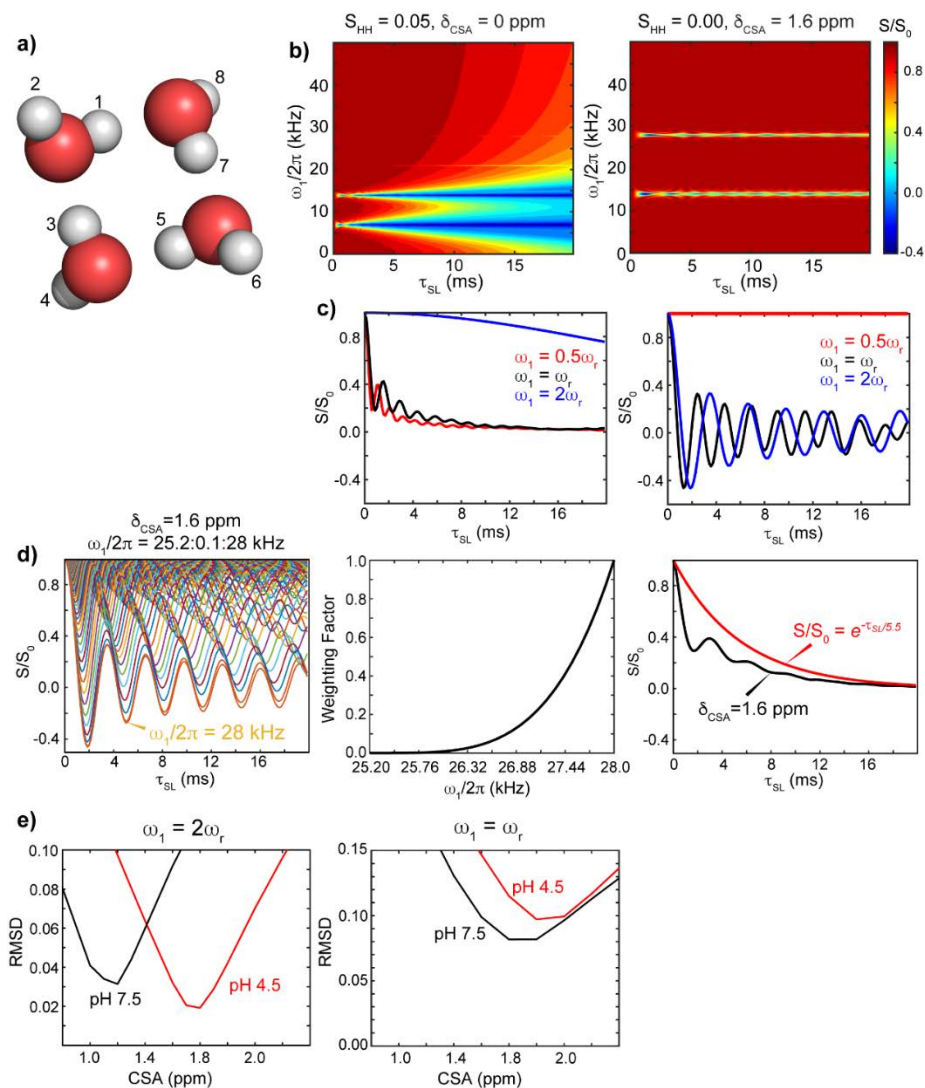
Supplementary Figure 5. Snapshots of representative water molecules near H19 over a 100 ps interval. **(a)** Closed channel represented by +0/+1 protonation for the H19/H27 tetrads. **(b)** Open channel represented by +4/+4 protonation for the H19/H27 tetrads.

Supplementary Figure 6. Numerical simulations and RMSD plots of the ^{1}H spin-lock recoupling experiment for extracting motionally averaged water ^{1}H CSA. (**a**) The spin system used in the simulations. The coordinates of eight protons in four water molecules were included. All ^{1}H spins were on resonance with the rf carrier frequency. All simulations were done for 14 kHz MAS on an 800 MHz spectrometer. Experiments began with *x*-magnetization and the amount of magnetization remaining on spin #1 was monitored as a function of spin-lock time. The water molecules are symmetric such that spins #1, #3, #5, and #7 are in the same magnetic environment and spins #2, #4, #6, and #8 are in the same magnetic environment. (**b**) (*left*) 2D dephasing map where ^{1}H-^{1}H dipolar couplings were included with an order parameter $S_{HH} = 0.05$ but CSA was neglected. The spin-lock mixing time, τ_{SL}, is plotted on the *x*-axis, and the spin-lock field strength ω_1 is shown on the *y*-axis. There are two broad matching conditions at $\omega_1 = 0.5\omega_r$ and ω_r. (*right*) 2D dephasing map in which a 1.6 ppm ^{1}H CSA was included for all protons, but ^{1}H-^{1}H dipolar couplings were neglected. There are two sharp matching conditions at $\omega_1 = \omega_r$ and $2\omega_r$. (**c**) Cross sections corresponding to spin-lock field strengths of $\omega_1 = 0.5\omega_r$, ω_r and $2\omega_r$ from ^{1}H-^{1}H dipolar coupling (*left*) and ^{1}H CSA (*right*) dephasing maps. Note that the ^{1}H-^{1}H dipolar couplings never

cause the signal to decay below zero. We note that the simulations in (**b**) and (**c**) depict the unrealistic condition of having no rf inhomogeneity, however they serve as an illustrative map of what rotary resonance matching conditions result in coherent recoupling for dipolar couplings and CSA. (**d**) (*left*) 50 recoupling curves simulated for the $\omega_1 = 2\omega_r$ condition plotted on one *xy*-plane to show the dispersion in the curve shapes and depths. Curves were simulated for rf field strengths corresponding to 90-100% of 28 kHz in 0.36% increments. (*middle*) Normalized x^4 weighting function that accounts for most of the sample experiencing the desired 28 kHz rf field strength, with only a miniscule fraction of the sample subjected to the 0.9*28 kHz inhomogeneity. (*right*) Exponential decay curve with a 5.5 ms relaxation time (*red*) to account for relaxation during the experiment. Final CSA recoupling curve for the $\omega_1 = 2\omega_r$ matching condition with a 1.6 ppm ^{1}H CSA (*black*) that accounts for rf inhomogeneity and relaxation. (**e**) Root-mean-square deviation (RMSD) between our experimental and simulated recoupling curves. We note that these fits used a 5.0 ms exponential relaxation time because this lead to the lowest RMSD's for both samples.
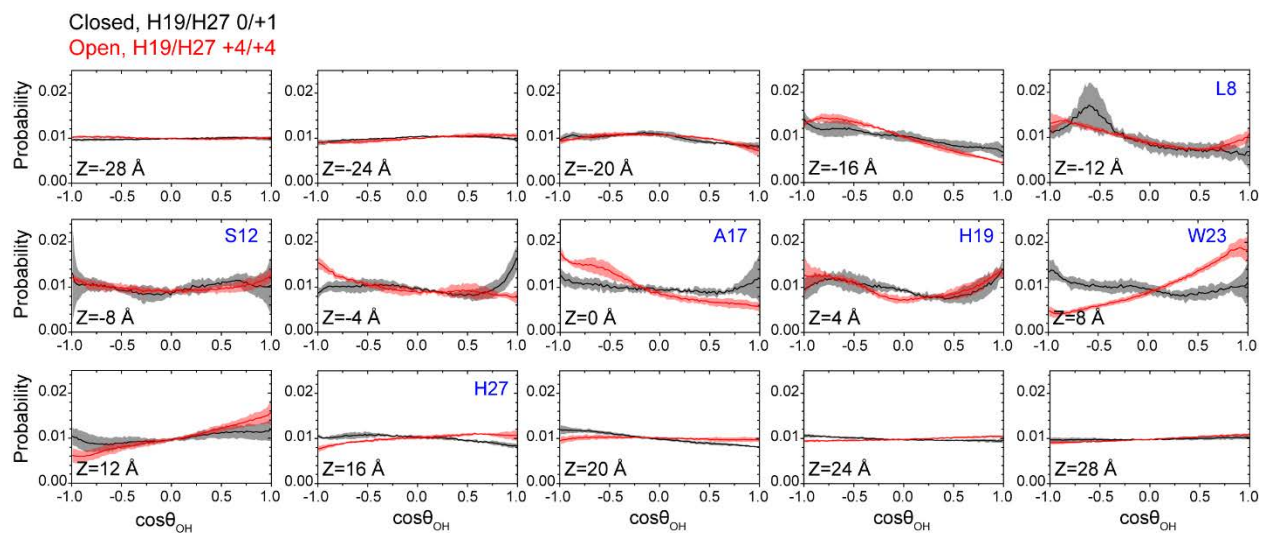
Supplementary Figure 7. Probability distributions of water order parameter $\cos\theta_{CH}$ along the channel axis in 4 Å bins. Lines and shaded areas show the mean and standard deviation, respectively, across the four replicates.
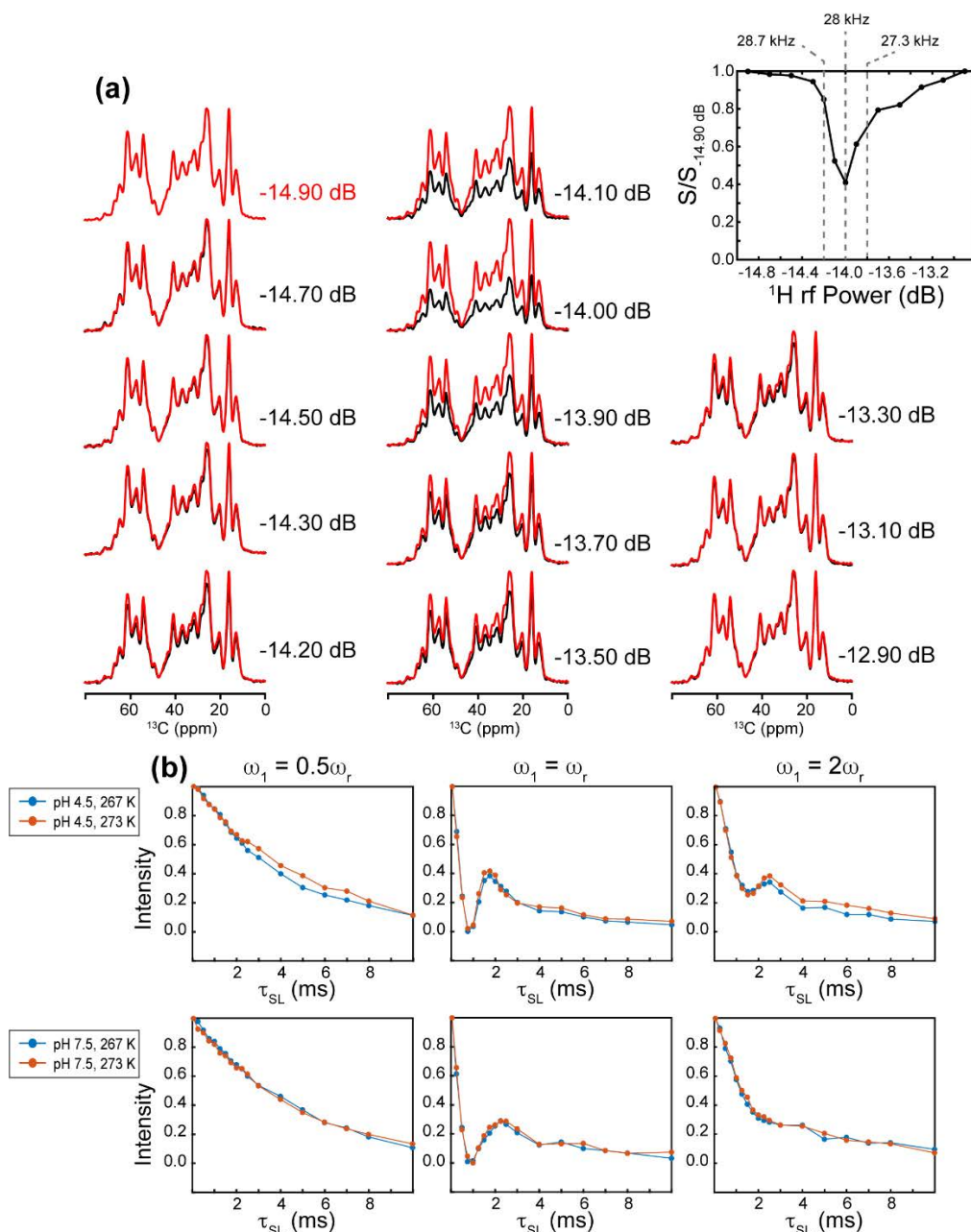
Supplementary Figure 8. (**a**) Experimental optimization of the ^{1}H spin-lock power for the $2\omega_r$ recoupling condition for the pH 4.5 sample. To optimize the rf power level, a minimum in the aliphatic intensity was found for a spin-lock recoupling time of 1 ms. This power level was optimized to within <0.1 dB, which would correspond to a 1.2% error in the applied rf power. (*upper right*) Integrated aliphatic intensity for the ^{1}H rf powers sampled in this optimization. The integrated intensity monotonically increases as the rf power is moved away from the optimal value. The same optimization routine was used to optimize the $2\omega_r$ matching condition for the pH 7.5 sample along with the $0.5\omega_r$ and ω_r matching conditions for both the pH 4.5 and pH 7.5 samples. (**b**) Comparison of ^{13}C-detected ^{1}H spin-lock recoupling experiments at sample temperatures of 273 K (**Fig. 5a**) and 267 K. We note that even though rotational motion and chemical exchange are expected to be slower at 267 K, we observe nearly identical recoupling curves.
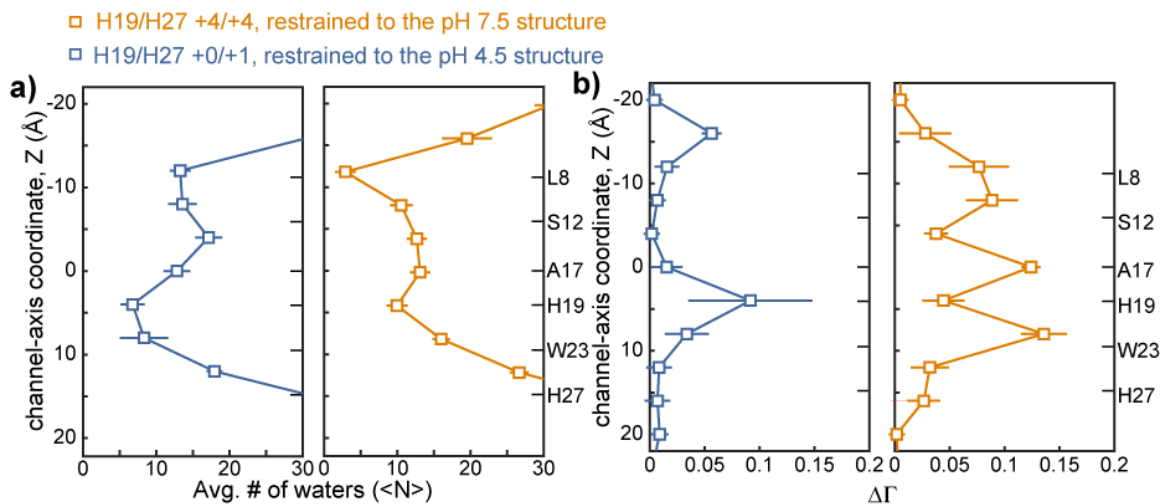
Supplementary Figure 9. Water simulations using +4/+4 charged H19/H27 tetrads restrained to the pH 7.5 solid-state NMR structure (PDB: 6PVR), and 0/+1 charged H19/H27 tetrads restrained to the pH 4.5 solid-state NMR structure (PDB: 6PVT). These unphysical conditions probe the relative effects of H19 charge and protein backbone conformation on channel-water dynamics. (**a**) Average number of water molecules in the channel. The +4/+4 state shows a large number of water molecules at the C-terminal H19-W23 juncture, even though the pH 7.5 structure with a tighter four-helix bundle is used for the simulations. (**b**) Entropy of $P(\cos(\theta_{OH}))$ distribution of channel water. The +4/4 state shows larger $\Delta\Gamma$, indicating larger water order.
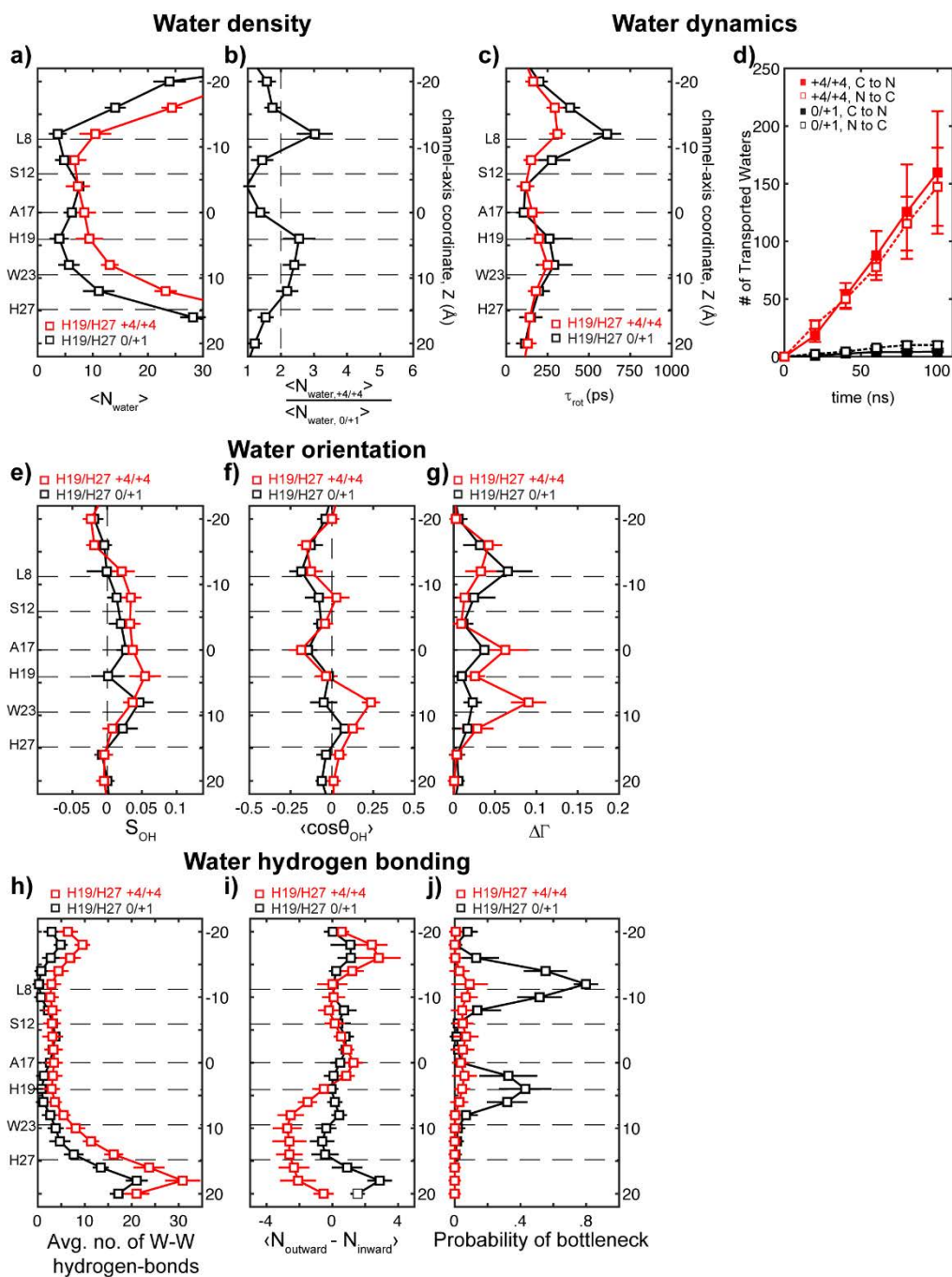
Supplementary Figure 10. Analysis of MD simulations performed at 297 K yield the same conclusions as the simulations at 277 K, presented in the main text. (**a**) Number of water molecules in the BM2 pore, for comparison with **Figure 2d**. (**b**) The ratio of water molecules in the +4/+4 state compared to the 0/+1 state, vertical guideline shows a ratio of 2 fold, for comparison with **Figure 2e**. The +4/+4 state has ~2 fold more water as compared to the 0/+1 state, in agreement with the result at 277K. (**c**) The rotational auto-correlation time, for comparison with **Figure 3f**. In agreement with the result at 277K, rotational dynamics are faster in the +4/+4 state (average τ_{rot} is 196±4 ps) as compared to the 0/+1 state (average τ_{rot} is 214±16 ps). As expected, rotational motion is found to be slightly faster overall at 297K as compared to 277K. (**d**) The number of

water molecules transported across the BM2 channel as a function of time, for comparison with **Figure 3g**. In agreement with the result at 277K, more water molecules are transported in the +4/+4 state (1.54±0.44 water/ns) as compared to the 0/+1 state (0.07±0.02 water/ns). As expected, transport is enhanced at 297K as compared to 277K. (**e**) OH-bond NMR order parameter, as determined from the MD trajectories, for comparison with **Figure 5c**. (**f**) The expectation value of the cosine of the OH-bond angle, for comparison with **Figure 5e**. In agreement with the result at 277K, a change in the orientational preference is observed around H19 in the +4/+4 state, but not in the 0/+1 state. (**g**) The entropy in the $P(\cos(\theta_{OH}))$ distribution, quantified using the parameter $\Delta\Gamma$ (see methods), for comparison with **Figure S4d**. In agreement with the result at 277K, water is more ordered in the +4/+4 state as compared to the 0/+1 state. (**h**) The average count of water-water hydrogen bonds is shown, for comparison with **Figure 7b**. In agreement with the 277 K result, the average hydrogen bond count is similar or larger along most of the channel for the the +4/+4 state state than for the 0/+1 state. (**i**) The average directionality metric is shown, for comparison to **Figure 7d**. In agreement with the 277 K result, there is more directionality in the +4/+4 state, with a shift in directionality at H19. (**j**) The bottleneck probability is shown, for comparison with **Figure 7c**. As for the 277 K simulations, bottlenecks are more more likely for the 0/+1 state than for the +4/+4 state.

Supplementary References

1.   Pattle, R.E. Diffusion from an Instantaneous Point Source with a Concentration-Dependent Coefficient. *Q. J. Mech. Appl. Math.* **12**, 407-409 (1959).
2.   Ader, C. et al. Structural Rearrangements of Membrane Proteins Probed by Water-Edited Solid-State NMR Spectroscopy. *J. Am. Chem. Soc.* **131**, 170-176 (2009).
3.   Sehgal, A.A., Duma, L., Bodenhausen, G. & Pelupessy, P. Fast proton exchange in histidine: measurement of rate constants through indirect detection by NMR spectroscopy. *Chem. Eur. J.* **20**, 6332-6338 (2014).
4.   Kateb, F., Pelupessy, P. & Bodenhausen, G. Measuring fast hydrogen exchange rates by NMR spectroscopy. *J. Magn. Resn.* **184**, 108-113 (2007).
5.   Liepinsh, E., Otting, G. & Wüthrich, K. NMR spectroscopy of hydroxyl protons in aqueous solutions of peptides and proteins. *J. Biomol. NMR* **2**, 447-465 (1992).
6.   Schanda, P. & Ernst, M. Studying Dynamics by Magic-Angle Spinning Solid-State NMR Spectroscopy: Principles and Applications to Biomolecules. *Prog. Nucl. Magn. Reson. Spectrosc.* **96**, 1-46 (2016).
7.   Palmer, A.G. & Massi, F. Characterization of the Dynamics of Biomacromolecules Using Rotating-Frame Spin Relaxation NMR Spectroscopy. *Chem. Rev.* **106**, 1700-1719 (2006).
8.   Liepinsh, E. & Otting, G. Proton exchange rates from amino acid side chains—implications for image contrast. *Mag. Reson. Med.* **35**, 30-42 (1996).
9.   Hu, F., Schmidt-Rohr, K. & Hong, M. NMR detection of pH-dependent histidine-water proton exchange reveals the conduction mechanism of a transmembrane proton channel. *J. Am. Chem. Soc.* **134**, 3703-3713 (2012).
10.   Nucci, N.V., Pometun, M.S. & Wand, A.J. Site-resolved measurement of water-protein interactions by solution NMR. *Nat. Struct. Mol. Biol.* **18**, 245-249 (2011).
11.   Gun'ko, V.M. & Turov, V.V. Structure of Hydrogen Bonds and 1H NMR Spectra of Water at the Interface of Oxides. *Langmuir* **15**, 6405-6415 (1999).
12.   Smith, A.A., Ernst, M. & Meier, B.H. Because the Light is Better Here: Correlation-Time Analysis by NMR Spectroscopy. *Angew. Chemie. Int. Ed.* **56**, 13590-13595 (2017).
13.   Smith, A.A., Ernst, M. & Meier, B.H. Optimized "detectors" for dynamics analysis in solid-state NMR. *J. Chem. Phys.* **148**, 045104 (2018).
14.   Bloembergen, N., Purcell, E.M. & Pound, R.V. Relaxation Effects in Nuclear Magnetic Resonance Absorption. *Phys. Rev.* **73**, 679-712 (1948).